Computers and Mathematics with Applications 175 (2024) 236–254

Contents lists available at ScienceDirect

Computers and Mathematics with Applications

journal homepage: www.elsevier.com/locate/camwa

Isogeometric analysis of the Laplace eigenvalue problem on circular sectors: Regularity properties and graded meshes

Thomas Apel, Philipp Zilk *

Institute for Mathematics and Computer-Based Simulation, Universität der Bundeswehr München, Werner-Heisenberg-Weg 39, 85577 Neubiberg, Germany

ARTICLE INFO

Dedicated to Professor Gundolf Haase on the occasion of his 60th birthday.

Keywords:
Isogeometric analysis
Eigenvalue problems
Corner singularities
Graded mesh refinement
Singular parameterizations
Circular sectors

ABSTRACT

The Laplace eigenvalue problem on circular sectors has eigenfunctions with corner singularities. Standard methods may produce suboptimal approximation results. To address this issue, a novel numerical algorithm that enhances standard isogeometric analysis is proposed in this paper by using a single-patch graded mesh refinement scheme. Numerical tests demonstrate optimal convergence rates for both the eigenvalues and eigenfunctions. Furthermore, the results show that smooth splines possess a superior approximation constant compared to their C^0-continuous counterparts for the lower part of the Laplace spectrum. This is an extension of previous findings about excellent spectral approximation properties of smooth splines on rectangular domains to circular sectors. In addition, graded meshes prove to be particularly advantageous for an accurate approximation of a limited number of eigenvalues. Finally, a hierarchical mesh structure is presented to avoid anisotropic elements in the physical domain and to omit redundant degrees of freedom in the vicinity of the singularity. Numerical results validate the effectiveness of hierarchical mesh grading for simulating eigenfunctions of low and high regularity.

1. Introduction

The Laplace eigenvalue problem

$$-\Delta u = \lambda u \quad \text{in } \Omega$$

on arbitrary domains $\Omega \subset \mathbb{R}^d$ is of great significance in numerous areas of applied mathematics. Not only is the Laplace spectrum itself crucial for many applications, e.g., due to the geometric information it contains [1,2], but it also appears during the analysis of other partial differential equations which describe everyday physical processes. For instance, the wave equation in two spatial dimensions describes the vibration of a membrane and its analytical solution can be derived by applying separation of variables and then solving the resulting Laplace eigenvalue problem [3]. For some one-, two- or three-dimensional model domains such as lines, rectangles, circular sectors or balls, the exact Laplace eigenvalues and eigenfunctions have been determined in the literature [4–6]. Yet, for more general domains, an analytical solution is usually not known and thus numerical methods are needed.

Isogeometric analysis (IGA) has been proven to provide powerful tools for an excellent approximation of the Laplace eigenvalues, especially in one dimension and for two-dimensional domains of rectangular nature [7–15]. However, the Laplace eigenfunctions of the underlying domains are always smooth and the question arises whether the spectrum of more complex domains, particularly in the presence of singularities and non-smooth eigenfunctions, can also be approximated well with IGA. For this purpose, circular sectors serve as a perfect model domain as they contain a typical corner singularity in the center and exact solutions of the Laplace eigenvalue problem are known such that spectral approximation properties can be verified numerically. In addition, one of the initial motivations of IGA can be explored during the discretization process: the exact representation of the computational domain geometry through the use of NURBS basis functions [16]. In this way, circular sectors can be parameterized exactly, which is not possible with finite elements [17].

Certainly, the corner singularity of circular sectors needs to be addressed during the numerical solution process to obtain a proper approximation of the Laplace spectrum. Many different approaches have been proposed in the literature and can be grouped into two categories. Either the mesh is locally refined towards the singularity or the approximation space is enriched by singular functions [18]. Sometimes, both ideas are combined. Within the framework of IGA, a method of the first category has been contributed where the parametric mapping is modified to obtain a grading of the mesh [19]. In a related work, which belongs to the first and second category, this idea has been combined with an en-

* Corresponding author.
E-mail addresses: thomas.apel@unibw.de (T. Apel), philipp.zilk@unibw.de (P. Zilk).

https://doi.org/10.1016/j.camwa.2024.09.018

Fig. 1. Circular sectors Ω with angle ω and the corresponding boundaries. (a) $\omega = \frac{3}{2}\pi$. (b) $\omega = 2\pi$.

richment of the basis by singular functions [20]. Another method of the first category is graded CutIGA where computational background meshes are cut arbitrarily to represent the singularity while retaining optimal approximation results [21]. Further possibilities include adaptive approaches or trimmed methods, both of which have gained significant attention in the field of isogeometric analysis recently, see for instance the overviews works [22,23].

The existing results about powerful spectral approximation properties have been achieved using standard single-patch IGA or very closely related methods. Therefore, we aim for an approach that is as close as possible to the standard method to maintain comparability between our results and the existing ones. In this context, we decide to use a method of the first category and we prefer to work with an exact representation of circular sectors instead of a trimmed approach. Since we consider a model problem where the location of the singularity is known, the local refinement can be set up a priori and there is no need for adaptive strategies which require more computational effort.

From finite element methods, it is well known that mesh grading is a simple and powerful tool for local a priori refinement towards corner singularities [24–27]. This idea has already been transferred to IGA by using a multi-patch approach [28]. However, the authors require the isogeometric mapping to be smooth, at least in the points towards which the mesh is locally refined. We contribute a new approach to overcome this restriction by using the single-patch polar-like parameterization of circular sectors which is singular at the conical point. Due to the singularity of the geometry mapping, a few basis functions that span the standard isogeometric approximation space are singular [29–31]. Approximation properties in such cases have so far only been shown for smooth functions on singularly parameterized triangles in [32]. Our contribution presents a numerical extension of this work to singularly parameterized circular sectors for a specific class of functions. Precisely, we consider numerical approximation properties for the set of eigenfunctions which possibly contains both smooth and singular functions depending on the angle of the circular sector.

The outline of this paper is as follows. In Section 2 we introduce the model problem, derive an analytical solution and investigate crucial regularity properties of the eigenfunctions. Section 3 contains a short overview about the basics of splines and NURBS and the corresponding notation which is then used in Section 4 to explain single-patch isogeometric mesh grading for circular sectors. In Section 5 we provide numerical results showing that the proposed method guarantees optimal convergence rates for the Laplace eigenpairs and hence is a powerful approach to solve the considered model problem. Moreover, we demonstrate that smooth splines are particularly useful on graded meshes for computing multiple eigenvalues and consider a combination with a hierarchical refinement scheme. In Section 6, we finally conclude our main findings and list some ideas for further research.

In the sequel, the symbol C is used for a generic positive constant, which may be different at each occurrence and is always independent of the mesh parameter h.

2. The Laplace eigenvalue problem on circular sectors

The main subject of this paper is the Laplace eigenvalue problem on circular sectors. Therefore, we provide the fundamental equations and boundary conditions, describe the analytical solutions and point out key regularity properties of the resulting eigenfunctions in this section.

2.1. The model problem

We consider the Laplace eigenvalue problem

$$\begin{aligned} -\Delta u &= \lambda u && \text{in } \Omega, \\ u &= 0 && \text{on } \Gamma_D, \\ \frac{\partial u}{\partial n} &= 0 && \text{on } \Gamma_N, \end{aligned} \tag{2.1}$$

where the model domain $\Omega = \{(r\cos\varphi, r\sin\varphi) \in \mathbb{R}^2 : 0 < r < 1, 0 < \varphi < \omega\}$ is a circular sector of angle $\omega \in (0, 2\pi]$. The Dirichlet boundary $\Gamma_D = \{(\cos\varphi, \sin\varphi) : 0 \le \varphi \le \omega\}$ consists of the circular edge and the Neumann boundary $\Gamma_N = \{(r\cos\varphi, r\sin\varphi) : 0 \le r < 1, \varphi \in \{0, \omega\}\}$ is given by the angle legs. We illustrate the model domain and its boundary for $\omega = \frac{3}{2}\pi$ and $\omega = 2\pi$ in Fig. 1.

From a physical point of view, the model problem (2.1) describes the vibrations of a membrane stretched over a circular sector. The membrane is assumed to be fixed at the circular Dirichlet boundary Γ_D. For $\omega = 2\pi$, we can think of a circular drum with a straight crack which is represented by the two angle legs. In this context, it is natural to choose Neumann boundary conditions on Γ_N. For the sake of simplicity, we stick to this choice of boundary conditions and do not discuss further combinations although our choice is not essential for the main findings of this paper.

2.2. Analytical solution

The analytical solution of our model problem (2.1) is well known and there is a vast amount of literature about it. According to Rayleigh, the theory of vibrations of a circular membrane has first been introduced by Clebsch [4,5]. Later, Rayleigh himself deduced the eigenmodes of circular sectors. We can not provide an exhaustive list here, but mention a few other works in which the problem has also been discussed [33,34]. In this section, we recapitulate the main findings. We adopt the notation used in the book [6, Chapter 10.2], where the vibrations of a circular membrane are derived in detail.

Let J_{ν_k} be the Bessel function to the order ν_k of the first kind and $\mu_{\nu_k,m}$ be the m-th root of J_{ν_k} for $m \in \mathbb{N}$. Then, the exact eigenfunctions can be expressed in polar coordinates by

$$u_{\nu_k,m}(r,\varphi) = a_{\nu_k,m}\, J_{\nu_k}(\mu_{\nu_k,m}\, r)\cos(\nu_k\, \varphi) \tag{2.2}$$

with $a_{\nu_k,m} \in \mathbb{R}$ and $\nu_k = k\frac{\pi}{\omega}$ for $k \in \mathbb{N}_0$. Throughout the paper, we set $a_{\nu_k,m} = 1$ for all $k \in \mathbb{N}_0$ and $m \in \mathbb{N}$ for the sake of simplicity and we call the functions (2.2) the Laplace eigenfunctions or eigenmodes of circular

sectors. The corresponding Laplace eigenvalues and eigenfrequencies of circular sectors are given by

$$\lambda_{\nu_k,m} = \mu_{\nu_k,m}^2 \quad \text{and} \quad \omega_{\nu_k,m} = \sqrt{\lambda_{\nu_k,m}} = \mu_{\nu_k,m}\,, \tag{2.3}$$

respectively. Ordering the eigenvalues and eigenfrequencies in ascending order, we denote them by λ_n and $\omega_n = \sqrt{\lambda_n}$ for $n = 1, 2, \dots$, respectively. The zeros of Bessel functions and their asymptotic behavior have been investigated extensively in the literature [34–39]. In particular, the sequences of eigenvalues $(\lambda_n)_{n\in\mathbb{N}}$ and eigenfrequencies $(\omega_n)_{n\in\mathbb{N}}$ satisfy

$$0 < \lambda_1 \le \lambda_2 \le \ldots \to \infty \quad \text{and} \quad 0 < \omega_1 \le \omega_2 \le \ldots \to \infty\,. \tag{2.4}$$

2.3. Regularity of the eigenfunctions

In this section, we delve into the regularity analysis of the Laplace eigenfunctions of circular sectors. To begin, we point out a useful representation of the considered eigenmodes.

Remark 2.1. The eigenfunctions (2.2) can be written in separated variables as a product

$$u_{\nu_k,m}(r,\varphi) = R(r)\,\Phi(\varphi) \tag{2.5}$$

of a smooth function $\Phi(\varphi) = \cos(\nu_k\,\varphi)$ satisfying $\left\|\Phi^{(l)}\right\|_{L^\infty(\Omega)} \le \nu_k^l$ for all $l \in \mathbb{N}_0$, and a Bessel function $R(r) = J_{\nu_k}(\mu_{\nu_k,m}\,r)$, which contains all the information about the regularity of the eigenfunctions. Typically, the solutions of boundary value problems on circular sectors are given by a sum of such products. Thus, the product form (2.5) is a particular property of the considered eigenvalue problem (2.1).

Motivated by Remark 2.1, we introduce some general properties of Bessel functions to investigate the regularity of the Laplace eigenfunctions (2.2). A useful asymptotic representation for small arguments of Bessel functions of the first kind to any order $\nu \notin \{-1, -2, -3, \dots\}$ is given by Abramowitz and Stegun [35, Formula 9.1.7, p. 360],

$$J_\nu(z) \sim \frac{1}{\Gamma(\nu_k+1)}\left(\frac{z}{2}\right)^\nu \quad \text{for } z \to 0\,. \tag{2.6}$$

As $\nu_k = k\,\frac{\pi}{\omega}$ for $k \in \mathbb{N}_0$, the formula (2.6) yields that every eigenfunction $u_{\nu_k,m}$ for $k \in \mathbb{N}_0$, $m \in \mathbb{N}$ satisfies

$$\begin{aligned} u_{\nu_k,m}(r,\varphi) = J_{\nu_k}(\mu_{\nu_k,m}\,r)\cos(\nu_k\,\varphi) &\sim \frac{1}{\Gamma(\nu_k+1)}\left(\frac{\mu_{\nu_k,m}\,r}{2}\right)^{\nu_k}\cos(\nu_k\,\varphi) \\ &= C r^{\nu_k} \quad \text{for } r \to 0\,. \end{aligned} \tag{2.7}$$

Hence, the Laplace eigenfunctions of circular sectors behave like the functions $r \mapsto r^{\nu_k}$ in the vicinity of the conical point, which is crucial to assess their regularity.

Furthermore, we have an integral representation of Bessel functions of the first kind to any order ν with $\mathrm{Re}(\nu) > -\frac{1}{2}$ [35, Chapter 9.1],

$$J_\nu(z) = \frac{\left(\frac{z}{2}\right)^\nu}{\pi^{1/2}\,\Gamma\left(\nu+\frac{1}{2}\right)}\int_0^\pi \cos(z\cos\theta)\sin^{2\nu}\theta\,\mathrm{d}\theta\,.$$

Thus, for $z \in \mathbb{R}$ with $z > 0$, it is

$$\left|J_\nu(z)\right| \le \frac{\left(\frac{z}{2}\right)^\nu}{\pi^{1/2}\,\Gamma\left(\nu+\frac{1}{2}\right)}\int_0^\pi \left|\sin^{2\nu}\theta\right|\,\mathrm{d}\theta = C(\nu)\,z^\nu \tag{2.8}$$

with $C(\nu) := \dfrac{\left(\frac{1}{2}\right)^\nu}{\pi^{1/2}\,\Gamma\left(\nu+\frac{1}{2}\right)}\displaystyle\int_0^\pi \left|\sin^{2\nu}\theta\right|\,\mathrm{d}\theta$. Combined with the asymptotic behavior (2.7), we obtain

$$\begin{aligned} \left|u_{\nu_k,m}(r,\varphi)\right| = \left|J_{\nu_k}(\mu_{\nu_k,m}\,r)\cos(\nu_k\,\varphi)\right| &\le C(\nu_k)\,(\mu_{\nu_k,m}\,r)^{\nu_k}\,\left|\cos(\nu_k\,\varphi)\right| \\ &\le C\,r^{\nu_k} \end{aligned} \tag{2.9}$$

in Ω for all $k \in \mathbb{N}_0$ and $m \in \mathbb{N}$.

Next, we consider the gradient $\nabla u = \left(\frac{\partial u}{\partial x_1}, \frac{\partial u}{\partial x_2}\right)^T$ of an eigenfunction $u = u_{\nu_k,m}$ for $k \in \mathbb{N}_0$, $m \in \mathbb{N}$ with x_1 and x_2 being Cartesian coordinates in $\mathbb{R}^2$. The eigenmodes can be differentiated using the recursion relation for Bessel functions [6, Chapter 10.5],

$$J_\nu'(z) = \frac{\nu}{z}J_\nu(z) - J_{\nu+1}(z)\,. \tag{2.10}$$

By changing to polar coordinates and setting $\mu = \mu_{\nu_k,m}$, it follows

$$\begin{aligned} |\nabla u| &\le C\left(\left|\frac{\partial u}{\partial r}\right| + \frac{1}{r}\left|\frac{\partial u}{\partial \varphi}\right|\right) \\ &= C\left(\left|\frac{\partial\left(J_{\nu_k}(\mu\,r)\right)}{\partial r}\cos(\nu_k\,\varphi)\right| + \frac{1}{r}\left|J_{\nu_k}(\mu\,r)\,\nu_k\,\sin(\nu_k\,\varphi)\right|\right) \\ &= C\left(\left|\left(\frac{\nu_k}{r}\,J_{\nu_k}(\mu\,r) - \mu\,J_{\nu_k+1}(\mu\,r)\right)\cos(\nu_k\,\varphi)\right|\right. \\ &\qquad \left. + \frac{1}{r}\left|J_{\nu_k}(\mu\,r)\,\nu_k\,\sin(\nu_k\,\varphi)\right|\right) \qquad (2.11) \\ &\le C\left(\frac{2\nu_k}{r}\left|J_{\nu_k}(\mu\,r)\right| + \mu\left|J_{\nu_k+1}(\mu\,r)\right|\right) \\ &\le C\left(\frac{2\nu_k}{r}(\mu r)^{\nu_k} + \mu(\mu r)^{\nu_k+1}\right) \\ &\le C\,r^{\nu_k-1} \qquad (2.12) \end{aligned}$$

with $C = C(\nu_k, m)$, where we use the bound (2.8) of the considered Bessel functions and $r \le 1$. We repeat the same argumentation for the higher derivatives

$$D^{\boldsymbol{\alpha}}u = \frac{\partial^{|\boldsymbol{\alpha}|}u}{\partial x_1^{\alpha_1}\,\partial x_2^{\alpha_2}} \quad \text{for multi-indices } \boldsymbol{\alpha} = \begin{pmatrix}\alpha_1\\ \alpha_2\end{pmatrix} \in \mathbb{N}_0^2$$

and obtain

$$\left|D^{\boldsymbol{\alpha}}u_{\nu_k,m}\right| \le C r^{\nu_k-|\boldsymbol{\alpha}|} \quad \text{in } \Omega \tag{2.13}$$

for all $k \in \mathbb{N}_0, m \in \mathbb{N}$ and $\boldsymbol{\alpha} \in \mathbb{N}_0^2$, where $|\boldsymbol{\alpha}| = \alpha_1 + \alpha_2$.

We are now able to determine the Sobolev regularity of the eigenmodes in the following lemma. Let $H^s(\Omega)$ for $s \in \mathbb{N}_0$ be the classical Sobolev spaces and $L^2(\Omega) = H^0(\Omega)$. For general $s \ge 0$ with $s \notin \mathbb{N}_0$ the notation $H^s(\Omega)$ is used for the Sobolev-Slobodeckij spaces.

Lemma 2.2. *Let $k \in \mathbb{N}_0$ and $m \in \mathbb{N}$. Then, the Laplace eigenfunctions of circular sectors (2.2) satisfy*

$$u_{\nu_k,m} \in H^s(\Omega) \quad \textit{for all } s \ge 0 \textit{ with } s < \nu_k + 1\,.$$

Proof. Estimate (2.13) shows that the eigenfunction $u_{\nu_k,m}$ and its derivatives can be controlled by the function $r \mapsto r^{\nu_k}$ and its derivatives. It is well known that $r \mapsto r^{\nu_k}$ is in $H^s(\Omega)$ for all $s \ge 0$ with $\nu_k - s > -1$, that is, for $s < \nu_k + 1$. □

In general, the regularity result in Lemma 2.2 is not sharp. For instance, consider $k = 0$. Then, it is $\nu_0 = 0$ and thus Lemma 2.2 only yields that $u_{\nu_0,m} \in H^s(\Omega)$ for all $s < 1$. Indeed, the eigenfunctions $u_{\nu_0,m}$ are of a different nature in the sense that

$$u_{\nu_k,m}(0,0) = \begin{cases} 1 & \text{if } k = 0\,, \\ 0 & \text{if } k > 0\,. \end{cases}$$

Nevertheless, it is clear that the functions $u_{\nu_0,m}$ are at least in $H^1(\Omega)$, since they are solutions of the weak form of our model problem (2.1),

which will be discussed more detailed in Section 2.5. In fact, Lemma 2.2 is sharp for all eigenmodes $u_{\nu_k,m}$ with $\nu_k \notin \mathbb{N}_0$, as the following lemma shows.

Lemma 2.3. *Let $k \in \mathbb{N}_0$ and $m \in \mathbb{N}$. The Laplace eigenfunctions of circular sectors (2.2) satisfy*

$$u_{\nu_k,m} \in H^s(\Omega) \quad \text{for all } s \geq 0$$

if and only if $\nu_k = k\frac{\pi}{\omega} \in \mathbb{N}_0$. For $\nu_k \notin \mathbb{N}_0$, the regularity result shown in Lemma 2.2 is sharp.

Proof. First, let $\nu_k = k\frac{\pi}{\omega} \notin \mathbb{N}_0$. Exploiting the asymptotic representation (2.7), we observe that $u_{\nu_k,m}$ behaves like $r \mapsto r^{\nu_k}$ for $r \to 0$. Consequently, it is $u_{\nu_k,m} \notin H^s(\Omega)$ for all $s \geq \nu_k + 1$ and Lemma 2.2 is sharp.

Now, let $n := \nu_k = k\frac{\pi}{\omega} \in \mathbb{N}_0$. Estimate (2.9) yields that

$$\left|u_{n,m}(r,\varphi)\right| = \left|J_n(\mu_{n,m}\, r)\cos(n\,\varphi)\right| \leq C r^n \left|\cos(n\,\varphi)\right| .$$

With the relations between Cartesian and polar coordinates, $(x, y) = (r\cos\varphi, r\sin\varphi)$ and $r^2 = x^2 + y^2$, it holds

$$\begin{aligned}
\left|u_{n,m}(r,\varphi)\right| &\leq C r^n \left|\cos(n\,\varphi)\right| \\
&= C r^n \left| \sum_{j=0}^{\lfloor \frac{n}{2} \rfloor} (-1)^j \binom{n}{2j} (\sin\varphi)^{2j} (\cos\varphi)^{n-2j} \right| \\
&= C \left| \sum_{j=0}^{\lfloor \frac{n}{2} \rfloor} (-1)^j \binom{n}{2j} r^{2j} (\sin\varphi)^{2j}\, r^{n-2j} (\cos\varphi)^{n-2j} \right| \\
&= C \left| \sum_{j=0}^{\lfloor \frac{n}{2} \rfloor} (-1)^j \binom{n}{2j} y^{2j}\, x^{n-2j} \right| \\
&= C \left| P_0(x,y) \right|
\end{aligned}$$

with the polynomial $P_0(x,y) := \sum_{j=0}^{\lfloor \frac{n}{2} \rfloor} (-1)^j \binom{n}{2j} y^{2j}\, x^{n-2j}$, where we used a multiple-angle formula for the cosinus [40, Chapter 2.6.2]. Hence, it is clear that $u \in L^2(\Omega)$. Next, we recall estimate (2.11) and apply a multiple-angle formula for the sinus [40, Chapter 2.6.2] to obtain

$$\begin{aligned}
|\nabla u_{n,m}| &\leq C \left(\left| \left(\frac{n}{r} J_n(\mu_{n,m}\, r) - \mu_{n,m}\, J_{n+1}(\mu_{n,m}\, r) \right) \cos(n\,\varphi) \right| \right. \\
&\qquad \left. + \frac{1}{r} \left| J_n(\mu_{n,m}\, r)\, n\, \sin(n\,\varphi) \right| \right) \\
&\leq C \left(\left(r^{n-1} - r^{n+1} \right) \left|\cos(n\,\varphi)\right| + r^{n-1} \left|\sin(n\,\varphi)\right| \right) \\
&\leq C r^{n-1} \left(\left|\cos(n\,\varphi)\right| + \left|\sin(n\,\varphi)\right| \right) \\
&= C r^{n-1} \left(\left| \sum_{j=0}^{\lfloor \frac{n}{2} \rfloor} (-1)^j \binom{n}{2j} (\sin\varphi)^{2j} (\cos\varphi)^{n-2j} \right| \right. \\
&\qquad \left. + \left| \sum_{j=0}^{\lfloor \frac{n-1}{2} \rfloor} (-1)^j \binom{n}{2j+1} (\sin\varphi)^{2j+1} (\cos\varphi)^{n-2j-1} \right| \right) \\
&\leq C r^{n-1} \left(\sum_{j=0}^{\lfloor \frac{n}{2} \rfloor} \binom{n}{2j} \left|\sin\varphi\right|^{2j} \left|\cos\varphi\right|^{n-2j} \right. \\
&\qquad \left. + \sum_{j=0}^{\lfloor \frac{n-1}{2} \rfloor} \binom{n}{2j+1} \left|\sin\varphi\right|^{2j+1} \left|\cos\varphi\right|^{n-2j-1} \right) \\
&\leq C r^{n-1} \left(\sum_{j=0}^{\lfloor \frac{n}{2} \rfloor} \binom{n}{2j} \left|\sin\varphi\right|^{2j-1} \left|\cos\varphi\right|^{n-2j} \right. \\
&\qquad \left. + \sum_{j=0}^{\lfloor \frac{n-1}{2} \rfloor} \binom{n}{2j+1} \left|\sin\varphi\right|^{2j} \left|\cos\varphi\right|^{n-2j-1} \right) \\
&= C \left(\sum_{j=0}^{\lfloor \frac{n}{2} \rfloor} \binom{n}{2j} \left|r\sin\varphi\right|^{2j-1} \left|r\cos\varphi\right|^{n-2j} \right. \\
&\qquad \left. + \sum_{j=0}^{\lfloor \frac{n-1}{2} \rfloor} \binom{n}{2j+1} \left|r\sin\varphi\right|^{2j} \left|r\cos\varphi\right|^{n-2j-1} \right) \\
&= C \left(\sum_{j=0}^{\lfloor \frac{n}{2} \rfloor} \binom{n}{2j} \left|x\right|^{2j-1} \left|y\right|^{n-2j} + \sum_{j=0}^{\lfloor \frac{n-1}{2} \rfloor} \binom{n}{2j+1} \left|x\right|^{2j} \left|y\right|^{n-2j-1} \right) \\
&\leq C P_1(|x|, |y|)
\end{aligned}$$

with the polynomial

$$P_1(x,y) = \sum_{j=0}^{\lfloor \frac{n}{2} \rfloor} \binom{n}{2j} x^{2j-1} y^{n-2j} + \sum_{j=0}^{\lfloor \frac{n-1}{2} \rfloor} \binom{n}{2j+1} x^{2j} y^{n-2j-1}.$$

Note that for some of the inequalities above it is essential that $r \in [0,1]$ and $|\sin\varphi| \in [0,1]$. Thus, it follows that $\nabla u_{n,m} \in L^2(\Omega)$ and $u_{n,m} \in H^1(\Omega)$. Similarly, for higher derivatives $D^{\boldsymbol{\alpha}} u_{n,m}$ for any multi-index $\boldsymbol{\alpha} \in \mathbb{N}_0^2$, there exists a polynomial $P_{|\boldsymbol{\alpha}|}$ such that

$$\left| D^{\boldsymbol{\alpha}} u_{n,m} \right| \leq C P_{|\boldsymbol{\alpha}|}(|x|, |y|) .$$

Therefore, it is $D^{\boldsymbol{\alpha}} u_{n,m} \in L^2(\Omega)$ for all $\boldsymbol{\alpha} \in \mathbb{R}^2$ and we obtain

$$u_{n,m} \in H^s(\Omega) \quad \text{for all } s \in \mathbb{N}_0 .$$

Using an interpolation argument for the Sobolev-Slobodeckij spaces, it immediately follows that $u_{n,m} \in H^s(\Omega)$ for all $s \geq 0$ and the lemma is proven. □

Throughout this paper, we will call the eigenfunctions $u_{\nu_k,m}$ with $\nu_k \in \mathbb{N}_0$ and $m \in \mathbb{N}$ smooth in the sense of Lemma 2.3. To conclude the regularity analysis, we derive some simple but illustrative conclusions from the two lemmata above.

Remark 2.4.

1. For all $k \in \mathbb{N}_0$ and $m \in \mathbb{N}$ it is $u_{\nu_k,m} \in H^1(\Omega)$.
2. The eigenfunctions $u_{\nu_0,m}$ of circular sectors with arbitrary angles $\omega \in (0, 2\pi]$ are smooth for all $m \in \mathbb{N}$.
3. Consider a circular sector whose angle ω satisfies $\frac{\pi}{\omega} \in \mathbb{N}$, that is, $\omega = \frac{\pi}{N}$ for some $N \in \mathbb{N}$. Then all its Laplace eigenfunctions $u_{\nu_k,m}$ are smooth as $\nu_k = k\frac{\pi}{\omega} \in \mathbb{N}$ for all $k \in \mathbb{N}_0$.
4. If the angle of a circular sector can not be expressed as a product of a rational number and π, i.e., $\omega \neq q\pi$ for all $q \in \mathbb{Q}$, it is $\nu_k = k\frac{\pi}{\omega} \notin \mathbb{N}$ for all $k \in \mathbb{N}$, that is, none of the eigenfunctions $u_{\nu_k,m}$ for $k > 0$ is smooth.
5. The eigenfunctions $u_{\nu_1,m}$ of circular sectors with angles $\omega \in (\pi, 2\pi]$ do not belong to $H^2(\Omega)$ for all $m \in \mathbb{N}$. They contain the strongest singularity among all eigenfunctions, which is of type r^{ν_1} near the conical point of the circular sector, where $\nu_1 = \frac{\pi}{\omega} \in \left[\frac{1}{2}, 1\right)$.

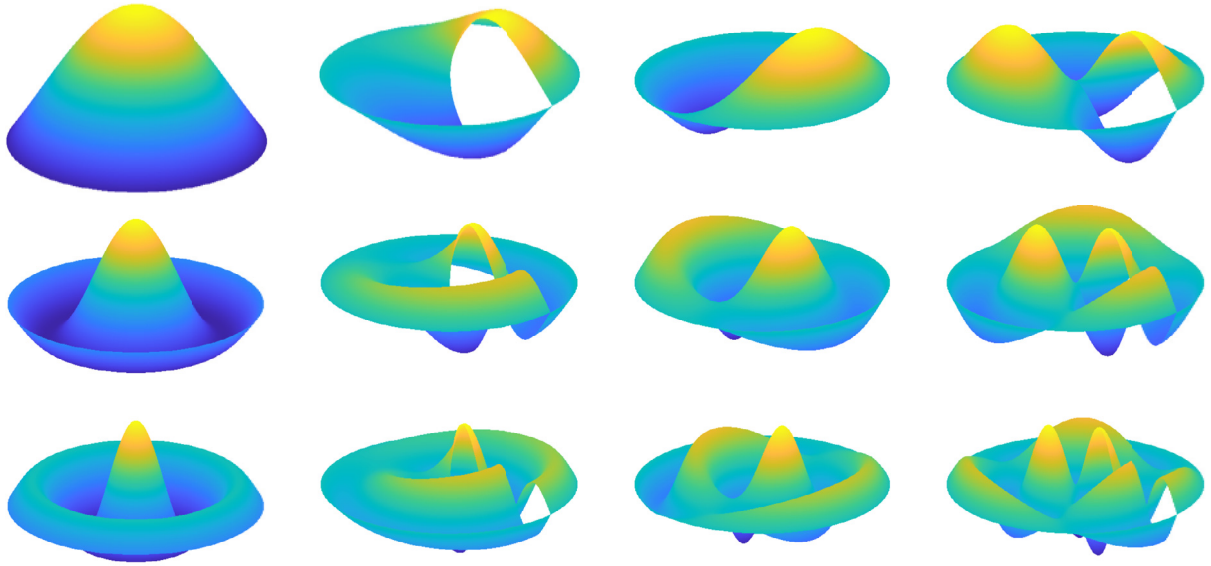

Fig. 2. Illustration of 12 Laplace eigenfunctions $u_{\nu_k,m}$ of the unit disk with crack. Columns from left to right: $\nu_k = 0, \nu_k = \frac{1}{2}, \nu_k = 1, \nu_k = \frac{3}{2}$. Rows from top to bottom: $m = 1, m = 2, m = 3$.

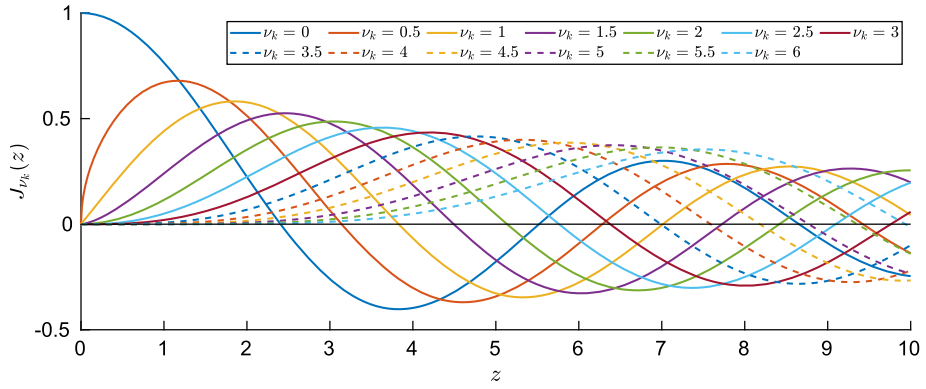

Fig. 3. Visualization of the Bessel functions J_{ν_k} to the orders $\nu_k \in \{0, 0.5, 1, \dots, 5.5, 6\}$ in the interval $[0, 10]$.

2.4. Eigenfunctions and eigenfrequencies of the unit disk with crack

To gain a deeper understanding of the model problem (2.1) and its exact solutions, we will now discuss a specific example: the circular sector with angle $\omega = 2\pi$, which represents the unit disk with a crack located along the positive x-axis, as presented in Fig. 1b. All other circular sectors with smaller angles $\omega < 2\pi$ can be interpreted as analogs or even simplifications of the case $\omega = 2\pi$.

The Laplace eigenfunctions of the unit disk with crack are given by the formula (2.2) with $\nu_k = \frac{k}{2}$ for $k \in \mathbb{N}_0$. Utilizing the regularity results outlined in Section 2.3, we categorize the eigenmodes into two types:

(A) $\nu_k \notin \mathbb{N}_0$, i.e., $k = 2n + 1$ for $n \in \mathbb{N}_0$. The corresponding eigenfunctions $u_{n+\frac{1}{2},m}$ have a singularity of type $r^{n+\frac{1}{2}}$ and are only contained in $H^s(\Omega)$ for all $s < n + \frac{3}{2}$, recall Lemma 2.2. As an example, the eigenmodes $u_{\nu_1,m}$ and $u_{\nu_3,m}$ for $m \in \{1, 2, 3\}$ have singularities of type $r^{1/2}$ and $r^{3/2}$, respectively, and are presented in the second and fourth columns of Fig. 2. It is noteworthy that the crack is clearly visible since the angular functions $\varphi \mapsto \cos(\nu_k \varphi) = \cos((n + \frac{1}{2})\varphi)$ are not 2π-periodic.

(B) $\nu_k \in \mathbb{N}_0$, i.e., $k = 2n$ for $n \in \mathbb{N}_0$. As indicated in Lemma 2.3, the corresponding eigenfunctions $u_{n,m}$ are smooth for all $m \in \mathbb{N}$. Exemplary eigenfunctions, namely $u_{\nu_0,m}$ and $u_{\nu_2,m}$ for $m \in \{1, 2, 3\}$, are showcased in the first and third columns of Fig. 2. Here, the crack is not visible in graphical representations of these eigenfunctions. This absence is due to the product form (2.5) of the eigenmodes and the 2π-periodicity of the angular functions $\varphi \mapsto \cos(\nu_k \varphi) = \cos(n\varphi)$.

As indicated in Remark 2.1, the regularity properties of the Laplace eigenmodes of circular sectors are based on the corresponding Bessel functions. In Fig. 3, we visualize the Bessel functions J_{ν_k} to the orders $\nu_k \in \{0, 1/2, 1, 3/2, \dots, 11/2, 6\}$, which are all the half-integer and integer Bessel functions with zeros in the interval $[0, 10]$. The asymptotic behavior (2.6) can be clearly observed, i.e., $J_{\nu_k}(z) \sim z^{\nu_k}$ for $z \to 0$, and J_0 differs from the other Bessel functions in the sense that $J_0(0) = 1$ and $J_{\nu_k}(0) = 0$ for $\nu_k \neq 0$. Bessel functions of half-integer order can be expressed explicitly [6, Chapter 10.5]. For instance, it holds

$$J_{\frac{1}{2}}(z) = \sqrt{\frac{2}{\pi z}} \sin z,$$

which once again highlights the presence of a singularity of type $z^{1/2}$ in the Bessel function $J_{\frac{1}{2}}$.

Table 1 provides the eigenfrequencies of the unit disk with crack within the interval $[0, 10]$, listed in ascending order. They are given by the zeros of the functions depicted in Fig. 3. Each eigenfrequency is associated with a specific root of a Bessel function, indicating the corresponding eigenfunction and its regularity. The eigenfrequencies ω_2, ω_8 and ω_{20}, highlighted in dark orange, correspond to eigenfunctions

Table 1
The eigenfrequencies (2.4) of the unit disk with crack are listed in ascending order within the interval $[0, 10]$. As per equation (2.3), each eigenfrequency corresponds to the m-th root of a Bessel function J_{ν_k}, denoted by $\omega_n = \mu_{\nu_k,m}$ for some $\nu_k \in \{0, 1/2, 1, 3/2, \dots\}$ and $m \in \mathbb{N}$. Additionally, the corresponding eigenfunctions and their regularity are provided, where $\varepsilon > 0$ is an arbitrarily small constant. Rows containing eigenfunctions with the strongest and second strongest singularity are highlighted in dark orange and light orange, respectively.

Eigenfrequency	Value	$\nu_k = k/2$	m	Eigenfunction	Regularity
ω_1	2.40	0	1	$u_{0,1}$	smooth
ω_2	3.14	1/2	1	$u_{1/2,1}$	$H^{3/2-\varepsilon}(\Omega)$
ω_3	3.83	1	1	$u_{1,1}$	smooth
ω_4	4.49	3/2	1	$u_{3/2,1}$	$H^{5/2-\varepsilon}(\Omega)$
ω_5	5.14	2	1	$u_{2,1}$	smooth
ω_6	5.52	0	2	$u_{0,2}$	smooth
ω_7	5.76	5/2	1	$u_{5/2,1}$	$H^{7/2-\varepsilon}(\Omega)$
ω_8	6.28	1/2	2	$u_{1/2,2}$	$H^{3/2-\varepsilon}(\Omega)$
ω_9	6.38	3	1	$u_{3,1}$	smooth
ω_{10}	6.99	7/2	1	$u_{7/2,1}$	$H^{9/2-\varepsilon}(\Omega)$
ω_{11}	7.02	1	2	$u_{1,2}$	smooth
ω_{12}	7.59	4	1	$u_{4,1}$	smooth
ω_{13}	7.73	3/2	2	$u_{3/2,2}$	$H^{5/2-\varepsilon}(\Omega)$
ω_{14}	8.18	9/2	1	$u_{9/2,1}$	$H^{11/2-\varepsilon}(\Omega)$
ω_{15}	8.42	2	2	$u_{2,2}$	smooth
ω_{16}	8.65	0	3	$u_{0,3}$	smooth
ω_{17}	8.77	5	1	$u_{5,1}$	smooth
ω_{18}	9.10	5/2	2	$u_{5/2,2}$	$H^{7/2-\varepsilon}(\Omega)$
ω_{19}	9.36	11/2	1	$u_{11/2,1}$	$H^{13/2-\varepsilon}(\Omega)$
ω_{20}	9.42	1/2	3	$u_{1/2,3}$	$H^{3/2-\varepsilon}(\Omega)$
ω_{21}	9.76	3	2	$u_{3,2}$	smooth
ω_{22}	9.94	6	1	$u_{6,1}$	smooth

with the strongest singularity, $u_{1/2,1}$, $u_{1/2,2}$ and $u_{1/2,3}$, respectively. Likewise, the frequencies ω_4 and ω_{13}, marked in light orange, belong to eigenfunctions with the second strongest singularity, $u_{3/2,1}$ and $u_{3/2,2}$, respectively, and so forth. Note that the occurrence of eigenfunctions characterized by identical singularities becomes rare as the frequencies increase. Loosely speaking, as $N \to \infty$, we observe that out of N^2 eigenfunctions, approximately N contain a singularity of type $r^{1/2}$, $r^{3/2}$, and so on.

2.5. Numerical solution process

Having explored the analytical solutions of the Laplace eigenvalue problem on circular sectors, we move on to the corresponding variational problem, which can be solved numerically by a Galerkin approach, see [3, Section I.3] for more details. The weak formulation of our model problem (2.1) reads: Find $(\lambda, u) \in \mathbb{R}^+ \times V_0 \setminus \{0\}$ such that

$$a(u, v) = \lambda\, b(u, v) \quad \forall v \in V_0\,, \tag{2.14}$$

where we define the spaces

$$V := H^1(\Omega) \quad \text{and} \quad V_0 := \{v \in V : v = 0 \text{ on } \Gamma_D\} \tag{2.15}$$

and the bilinear forms

$$a : V \times V \to \mathbb{R}, \quad a(u, v) := \int_\Omega \nabla u \cdot \nabla v \, \mathrm{d}\boldsymbol{x}\,,$$

$$b : V \times V \to \mathbb{R}, \quad b(u, v) := \int_\Omega u\, v \, \mathrm{d}\boldsymbol{x}\,.$$

Since both bilinear forms are bounded and a is coercive on V_0, the eigenvalue problem (2.14) has an infinite sequence of eigenvalues [3, Section I.4]

$$0 < \lambda_1 \le \lambda_2 \le \cdots \nearrow +\infty$$

and corresponding eigenfunctions $u_1, u_2, \dots \in V_0$.

Let further $V_{0h} \subset V_0$ be an l-dimensional subspace. The corresponding discrete eigenvalue problem reads: Find $(\lambda_h, u_h) \in \mathbb{R}^+ \times V_{0h} \setminus \{0\}$ such that

$$a(u_h, v_h) = \lambda_h\, b(u_h, v_h) \quad \forall v_h \in V_{0h}\,, \tag{2.16}$$

which yields a finite sequence of eigenvalues [3, Chapter 5]

$$0 < \lambda_{1,h} \le \lambda_{2,h} \le \cdots \le \lambda_{l,h}$$

and corresponding eigenfunctions $u_{1,h}, u_{2,h}, \dots, u_{l,h} \in V_{0h}$. Since V_{0h} is finite-dimensional, the discrete problem (2.16) is equivalent to a generalized matrix eigenvalue problem. The resulting discrete eigenfunctions and eigenvalues converge to the continuous ones for $h \to 0$ if the spaces V_{0h} are chosen appropriately. While finite element methods (FEM) typically employ continuous piecewise polynomials, IGA makes use of B-splines and NURBS, a class of functions that will be introduced in the following section.

3. Basics of isogeometric analysis

We present the essential basics of isogeometric analysis and establish necessary notation, largely following the framework presented in the review paper [41]. A more detailed introduction can be found in the books [9] on isogeometric analysis and [42] on spline theory.

3.1. Univariate B-splines and NURBS

First, we introduce the concept of B-splines and NURBS in the univariate case and provide a brief overview of common refinement procedures. Let $p \in \mathbb{N}_0$ and $n \in \mathbb{N}$. We call $\Xi := \{\xi_1, \xi_2, \dots, \xi_{n+p+1}\}$ a p-open knot vector if

$$\xi_1 = \cdots = \xi_{p+1} < \xi_{p+2} \le \xi_{p+3} \le \cdots \le \xi_{n-1} \le \xi_n < \xi_{n+1} = \cdots = \xi_{n+p+1}\,,$$

where $\xi_i \in \mathbb{R}$ for $i = 1, \dots, n+p+1$ is called the i-th knot which is allowed to occur repeatedly. Without loss of generality, we assume that $\xi_1 = 0$ and $\xi_{n+p+1} = 1$ and hence all the knots are contained in the unit interval $[0, 1]$. Furthermore, we define the vector $Z = \{\zeta_1, \dots, \zeta_N\}$ of knots without repetitions, also called breakpoints, with

$$\Xi = \{\underbrace{\zeta_1, \dots, \zeta_1}_{m_1 \text{ times}}, \underbrace{\zeta_2, \dots, \zeta_2}_{m_2 \text{ times}}, \dots, \underbrace{\zeta_N, \dots, \zeta_N}_{m_N \text{ times}}\}\,,$$

where $N \in \mathbb{N}$ is the total number of pairwise different knots and $m_j \in \mathbb{N}$ for $j = 1, \dots, N$ denotes the multiplicity of the breakpoint ζ_j such that $\sum_{j=1}^N m_j = n + p + 1$. For p-open knot vectors, $m_1 = m_N = p + 1$ always holds, and we assume $m_j \le p + 1$ for the internal knot multiplicities. The entries of Z define a mesh on the unit interval $[0, 1]$.

From the given knot vector, B-spline basis functions of degree p, denoted by

$$\widehat{B}_{i,p} : [0, 1] \to \mathbb{R}, \quad \zeta \mapsto \widehat{B}_{i,p}(\zeta)\,, \quad i = 1, 2, \dots, n\,,$$

can be constructed using the iterative scheme as explained, for instance, in [9, Section 2.1]. They build a basis of the space of splines on the subdivision Z, that is, piecewise polynomials of degree p with $p - m_j$ continuous derivatives at the breakpoints ζ_j, $j = 1, \dots, N$. Besides other characteristics, the B-spline basis functions are non-negative and form a partition of unity.

Classical splines face restrictions in representing important geometries like conic sections. To overcome this limitation, non-uniform rational B-splines (NURBS) are introduced, see [43] for more details. Therefore, the weight function

$$W(\zeta) = \sum_{l=1}^{n} w_l\, \widehat{B}_{l,p}(\zeta)$$

is determined by choosing positive constants $w_l > 0$, $l = 1, \dots, n$, which are called weights. The NURBS basis functions are then defined by

$$\widehat{N}_{i,p}(\zeta) = \frac{w_i \widehat{B}_{i,p}(\zeta)}{\sum_{l=1}^{n} w_l \widehat{B}_{l,p}(\zeta)} = \frac{w_i \widehat{B}_{i,p}(\zeta)}{W(\zeta)}, \quad i = 1, \dots, n.$$

We denote the corresponding NURBS space by

$$N_p(\Xi, W) = \operatorname{span}\left\{ \widehat{N}_{i,p} : i = 1, \dots, n \right\}.$$

The NURBS spaces can be refined through knot insertion and degree elevation. In total, three refinement types can be constructed by combining the algorithms. Knot insertion results in the classical mesh refinement known as h-refinement, while degree elevation enables p-refinement. Consecutive application of degree elevation and knot insertion is called k-refinement. This approach allows to maintain the regularity at the internal knots of Ξ^0 while enhancing differentiability at all other knots. For a more detailed description of these refinement procedures we refer the interested reader to [16], where they were initially introduced.

3.2. Bivariate B-splines and NURBS

Multivariate B-splines and NURBS are constructed as tensor products of their univariate counterparts. This section provides a summary of the main concepts and notation. The focus of our paper is on the analysis of circular sectors, so we set the spatial dimension $d = 2$ and specifically consider bivariate B-splines and NURBS. However, all definitions and notations can be easily extended to higher dimensions.

Let $n_l \in \mathbb{N}$, the degrees $p_l \in \mathbb{N}$ and the p_l-open knot vectors $\Xi_l = \{\xi_{l,1}, \xi_{l,2} \dots, \xi_{l,n_l+p+1}\}$ be given for $l = 1, 2$. We define the polynomial degree vector $\boldsymbol{p} = (p_1, p_2)$ and the bivariate knot vector $\boldsymbol{\Xi} = \Xi_1 \times \Xi_2$. Further, let $N_l \in \mathbb{N}$ be the number of knots without repetition for each direction such that the corresponding univariate knot vectors of breakpoints are given by $Z_l = \{\zeta_{l,1}, \zeta_{l,2} \dots, \zeta_{l,N_l}\}$ for $l = 1, 2$. They form a Cartesian grid in the parametric domain $\widehat{\Omega} = (0,1)^2$, which defines the parametric Bézier mesh $\widehat{\mathcal{M}}$,

$$\widehat{\mathcal{M}} := \left\{ Q_{\boldsymbol{j}} \subset \widehat{\Omega} : Q_{\boldsymbol{j}} = Q_{(j_1,j_2)} = (\zeta_{1,j_1}, \zeta_{1,j_1+1}) \times (\zeta_{2,j_2}, \zeta_{2,j_2+1}), \boldsymbol{j} \in \boldsymbol{J} \right\}, \tag{3.1}$$

where we introduce the set of multi-indices $\boldsymbol{J} = \{\boldsymbol{j} = (j_1, j_2) : 1 \le j_l \le N_l - 1, l = 1, 2\}$.

Bivariate B-spline functions are then defined by

$$\widehat{B}_{\boldsymbol{i},\boldsymbol{p}} : [0,1]^2 \to \mathbb{R}, \quad \widehat{B}_{\boldsymbol{i},\boldsymbol{p}}(\boldsymbol{\zeta}) = \widehat{B}_{i_1,p_1}(\zeta_1)\, \widehat{B}_{i_2,p_2}(\zeta_2)$$

for $\boldsymbol{i} \in \boldsymbol{I} = \{\boldsymbol{i} = (i_1, i_2) : 1 \le i_l \le n_l, l = 1, 2\}$. The corresponding bivariate NURBS basis functions read

$$\widehat{N}_{\boldsymbol{i},\boldsymbol{p}}(\boldsymbol{\zeta}) = \frac{w_{\boldsymbol{i}}\, \widehat{B}_{\boldsymbol{i},\boldsymbol{p}}(\boldsymbol{\zeta})}{W(\boldsymbol{\zeta})}$$

using the weight function

$$W(\boldsymbol{\zeta}) = \sum_{\boldsymbol{l} \in \boldsymbol{I}} w_{\boldsymbol{l}}\, \widehat{B}_{\boldsymbol{l},\boldsymbol{p}}(\boldsymbol{\zeta}), \tag{3.2}$$

where we choose weights $w_{\boldsymbol{l}} > 0$ for all $\boldsymbol{l} \in \boldsymbol{I}$. The space of NURBS on the parametric domain is finally denoted by

$$N_{\boldsymbol{p}}(\boldsymbol{\Xi}, W) = \operatorname{span}\left\{ \widehat{N}_{\boldsymbol{i},\boldsymbol{p}}(\boldsymbol{\zeta}), \boldsymbol{i} \in \boldsymbol{I} \right\}$$

and the univariate refinement algorithms mentioned in Section 3.1 can be generalized to the bivariate case.

NURBS surfaces in $\mathbb{R}^m$, $m = 2, 3$, are defined as linear combinations of the tensor product functions introduced above,

$$\boldsymbol{F}(\boldsymbol{\zeta}) = \sum_{\boldsymbol{i} \in \boldsymbol{I}} \boldsymbol{c}_{\boldsymbol{i}} \widehat{N}_{\boldsymbol{i},\boldsymbol{p}}(\boldsymbol{\zeta}), \tag{3.3}$$

where each basis function is associated with a control point $\boldsymbol{c}_{\boldsymbol{i}} \in \mathbb{R}^m$, $\boldsymbol{i} \in \boldsymbol{I}$. The $\boldsymbol{F}$-image $\Omega = \boldsymbol{F}(\widehat{\Omega})$ of the parametric domain $\widehat{\Omega} = (0,1)^2$ is commonly referred to as the physical domain. Using this construction, exact parameterizations

$$\boldsymbol{F} : \widehat{\Omega} \to \Omega$$

of various types of domains $\Omega \subset \mathbb{R}^2$, including circular sectors, can be obtained. For further details, the interested reader may consult the books [9,43,44].

To define a mesh in Ω, we consider the image under $\boldsymbol{F}$ of the partition given by the knot vectors without repetitions, i.e., each element $Q_{\boldsymbol{j}} \in \widehat{\mathcal{M}}$ of the parametric Bézier mesh from (3.1) is mapped to an element $K_{\boldsymbol{j}} = \boldsymbol{F}(Q_{\boldsymbol{j}})$ in the physical domain. We set

$$\mathcal{M} := \left\{ K_{\boldsymbol{j}} \subset \Omega : K_{\boldsymbol{j}} = \boldsymbol{F}(Q_{\boldsymbol{j}}), \boldsymbol{j} \in \boldsymbol{J} \right\},$$

which is commonly known as the physical Bézier mesh, or simply Bézier mesh. The meshes for the coarsest knot vector Ξ^0 will be denoted by $\widehat{\mathcal{M}}_0$ and $\mathcal{M}_0$.

4. Isogeometric mesh grading for circular sectors

In the following, we demonstrate explicitly how the constructions presented in Section 3 can be used to address the numerical solution of our model problem (2.1) with isogeometric analysis. We begin by describing the single-patch polar-like NURBS parameterization of circular sectors and discuss the resulting spline spaces on the computational domain. The standard spaces go beyond the solution space of the weak problem (2.14) due to the low regularity of the parameterization, which results in a variational crime [29]. To circumvent this, a modified approximation space is employed. Finally, we propose a graded mesh refinement scheme to tackle the singularities of the eigenfunctions observed in Section 2.3 and explore the choice of the associated grading parameter.

Here, we concentrate again on the circular sector Ω with angle $\omega = 2\pi$, as illustrated in Fig. 1b, which represents a unit disk with a crack on the positive x-axis. Just as in Section 2.4, it serves as a prototype for all other circular sectors with smaller angles $\omega < 2\pi$, where the same procedure can be carried out in an analogous or even simplified manner.

4.1. Single-patch parameterization and coarse meshes

First, we construct the single-patch polar-like isogeometric parameterization $\boldsymbol{F} : \widehat{\Omega} \to \Omega$ of the unit disk with crack. The approach can be described intuitively by the deformations shown in Fig. 4a and has been employed similarly in [20]. We combine the typical 9-point NURBS discretization of circles with a linear component in radial direction. Various other possibilities for parameterizing circular sectors and disks have been studied in the literature [17,29,45–47]. In particular, we use the open knot vectors

$$\Xi_1^0 = \{0, 0, 1, 1\} \quad \text{and} \quad \Xi_2^0 = \left\{0, 0, 0, \tfrac{1}{4}, \tfrac{1}{4}, \tfrac{1}{2}, \tfrac{1}{2}, \tfrac{3}{4}, \tfrac{3}{4}, 1, 1, 1\right\} \tag{4.1}$$

along with the control points $\boldsymbol{c}_{\boldsymbol{i}}$ as illustrated in Fig. 4b and the standard weights $w_{\boldsymbol{i}}$ for $\boldsymbol{i} \in \boldsymbol{I}_0 = \{(i_1, i_2) : 1 \le i_1 \le 2, 1 \le i_2 \le 9\}$. Note that all the control points $\boldsymbol{c}_{(1,i_2)}$ for $i_2 = 1, \dots, 9$ lie at the conical point $\boldsymbol{S} = (0,0)$ of the circular sector, causing the parametric edge $\{(0, \zeta_2) : \zeta_2 \in [0,1]\}$ to collapse to this point in the physical domain. The corresponding edge is depicted in cyan in Fig. 4a and will be referred to as the singular edge of $\widehat{\Omega}$ in this paper. We further direct the interested reader to Appendix A for an explicit representation of the parameterization $\boldsymbol{F}$ and to Appendix B for a comparison of $\boldsymbol{F}$ to the classic transformation between Cartesian and polar coordinates.

The vectors of knots without repetitions,

$$Z_1 = \{0, 1\} \quad \text{and} \quad Z_2 = \left\{0, \tfrac{1}{4}, \tfrac{1}{2}, \tfrac{3}{4}, 1\right\},$$

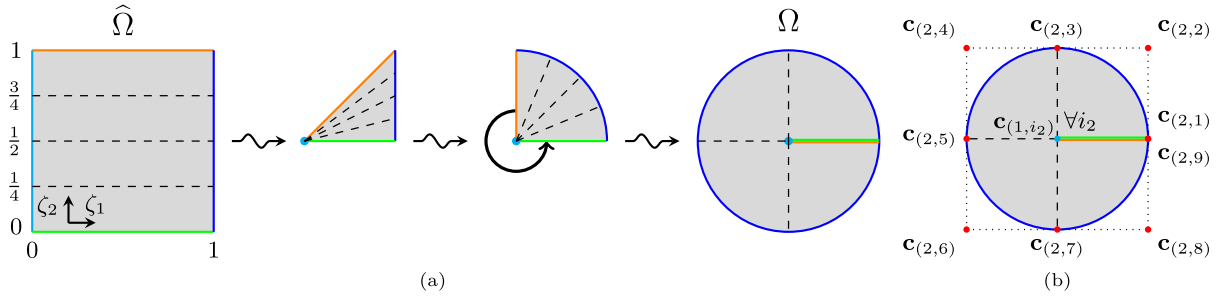

Fig. 4. (a) Deforming a unit square to a unit disk with crack. (b) Illustration of the control points $\boldsymbol{c}_i$ for $\boldsymbol{i} \in \boldsymbol{I}_0 = \{\boldsymbol{i} = (i_1, i_2) : 1 \le i_1 \le 2, 1 \le i_2 \le 9\}$.

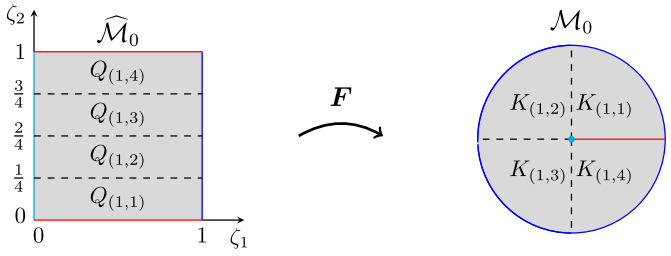

Fig. 5. Illustration of the coarse parametric Bézier mesh (4.2) and the corresponding physical Bézier mesh (4.3).

form a Cartesian grid which defines the coarse parametric Bézier mesh

$$\widehat{\mathcal{M}}_0 := \left\{ Q_{(1,j_2)} = (0,1) \times \left(\frac{j_2 - 1}{4}, \frac{j_2}{4} \right) : 1 \le j_2 \le 4 \right\}. \tag{4.2}$$

With identity (B.1) from Appendix B, it follows that

$$\begin{aligned} K_{(1,j_2)} &= \boldsymbol{F}(Q_{(1,j_2)}) \\ &= \left\{ (r\cos\varphi, r\sin\varphi) \in \mathbb{R}^2 : r \in (0,1), \varphi \in \left(\frac{j_2 - 1}{2}\pi, \frac{j_2}{2}\pi \right) \right\} \end{aligned}$$

for $j_2 = 1, \dots, 4$. We obtain the coarse physical Bézier mesh

$$\mathcal{M}_0 := \left\{ K_{(1,j_2)} : 1 \le j_2 \le 4 \right\}. \tag{4.3}$$

Both meshes are illustrated in Fig. 5.

4.2. Standard isogeometric approximation spaces

To establish a comprehensive framework for the numerical solution of model problem (2.1), we proceed to describe the isogeometric approximation spaces. Adopting an isoparametric approach, we use the discrete function space that defines the parameterization $\boldsymbol{F}$ also for the approximation space.

We begin with the coarse bivariate NURBS space in the parametric domain, as defined in Section 3.2,

$$N_{p^0}(\Xi^0, W) = \operatorname{span}\left\{ \widehat{N}_{i,p^0}(\boldsymbol{\zeta}), \boldsymbol{i} \in \boldsymbol{I}_0 \right\},$$

where $\Xi^0 = \Xi_1^0 \times \Xi_2^0$ and $\boldsymbol{p}^0 = (p_1^0, p_2^0) = (1,2)$. By applying the classical refinement algorithms introduced in Section 3.1, we can construct finer parametric spaces $N_p(\Xi, W)$ with $N_{p^0}(\Xi^0, W) \subset N_p(\Xi, W)$.

NURBS spaces in the physical domain are typically defined by the $\boldsymbol{F}$-image of the parametric spaces [41,48,49]. More precisely, if $\widehat{V}_h = N_p(\Xi, W) = \operatorname{span}\{\widehat{N}_{i,p}(\boldsymbol{\zeta}), \boldsymbol{i} \in \boldsymbol{I}\}$ is a refinement of the coarse parametric NURBS space $N_{p^0}(\Xi^0, W)$, the approximation space in the physical domain is defined by

$$V_h = \left\{ f \circ \boldsymbol{F}^{-1} : f \in \widehat{V}_h \right\}.$$

A basis of this space can be provided by a push-forward of the parametric basis,

$$V_h = \operatorname{span}\left\{ N_{\boldsymbol{i},\boldsymbol{p}}(\boldsymbol{x}) := \widehat{N}_{\boldsymbol{i},\boldsymbol{p}} \circ \boldsymbol{F}^{-1}(\boldsymbol{x}), \boldsymbol{i} \in \boldsymbol{I} \right\}. \tag{4.4}$$

However, this approach requires certain regularity assumptions on the parameterization, for more details see [41]. These requirements are not fulfilled by the polar-like mapping that we constructed in Section 4.1. Hence, the approximation space (4.4) needs to be modified which will be investigated in detail in the next section.

4.3. Modification of the approximation space due to the singular parameterization

It has been shown in [29,30] that the lack of regularity in the isogeometric parameterization results in some of the basis functions (4.4) not belonging to $H^1(\Omega)$, which implies $V_h \not\subset H^1(\Omega)$. As outlined in Section 2.5, this constitutes a violation of Galerkin's principle since the discrete space is required to be a subset of the solution space, i.e., $V_h \subset V = H^1(\Omega)$. Therefore, we employ the modified approximation space proposed in [29], see also [50],

$$V_h^s := V_h \cap H^1(\Omega).$$

A corresponding basis can be constructed by replacing all the basis functions associated to the control points collapsing in the conical point of the circular sector with a single function consisting of their sum. Moreover, we also have to take the boundary conditions into account and obtain the final approximation space

$$V_{0h}^s = V_h^s \cap V_0$$

with V_0 from (2.15).

Remark 4.1. The modification of the approximation space results in an intervention in standard isogeometric analysis. Our approach can also be set up without this modification, accepting that a variational crime is committed. It turns out that the method still proves effective and the numerical results are very similar, see [51].

Remark 4.2. As mentioned in Section 4.1, there exist several other ways to parameterize circular sectors than using the polar-like mapping $\boldsymbol{F}$. In particular, a multi-patch approach based on biquadratic NURBS can be employed, which has been proposed in the numerical examples of [28]. The multi-patch parameterization contains another type of singularities which are located on the circular boundary [29]. Hence, the singularity of the Laplace eigenfunctions does not coincide with the singularities of the isogeometric mapping, which may simplify the problem. However, we prefer the presented single-patch approach for the following reasons:

- As indicated in Section 1, previous results about spectral approximation properties of IGA in the literature have been shown for single-patch domains.
- A polar-like discretization seems to be more natural and intuitive when considering circular sectors in an isogeometric context.

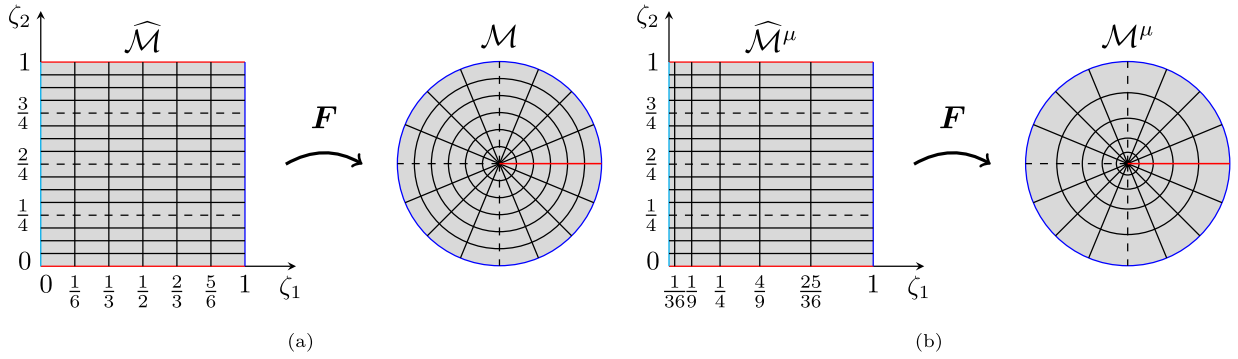

Fig. 6. Parametric and physical Bézier meshes $\widehat{\mathcal{M}}$ and $\mathcal{M}$ after refining with $J_1 = 6$ and $J_2 = 16$. Solid black lines are used for new subdivisions and dashed black lines for the initial coarse meshes $\widehat{\mathcal{M}}_0$ and $\mathcal{M}_0$. (a) Uniform refinement (b) Graded refinement with grading parameter $\mu = 1/2$.

- The multi-patch approach leads to redundant control points at the patch junctions which are absent when using only one singularly mapped patch.
- Introducing a numerical framework becomes more complicated when multiple patches are used instead of a single one. Besides, standard approximation theory for IGA can not be applied. Even though the singularities in the multi-patch parameterization of circular sectors are weaker than the singularity in our single-patch mapping $\boldsymbol{F}$, the necessary regularity assumptions, as discussed in [41,48], are not fulfilled. Up to our knowledge, the multi-patch discretization of circular sectors has only been considered numerically so far, but not in the error analysis [28].

4.4. Single-patch mesh grading

After setting up the isogeometric framework for the numerical solution of our model problem (2.1), we now propose a modified refinement algorithm to tackle the singularities of the Laplace eigenfunctions discussed in Section 2.3.

4.4.1. Graded mesh refinement scheme

Isogeometric h-refinement is achieved through knot insertion, recall Section 3.1. In standard IGA, the univariate knot vectors are refined uniformly, with newly inserted knots being equidistantly distributed. We propose a more flexible knot insertion method that allows local mesh refinement towards known singularities. The key concept is to abandon uniformity in favor of knots concentrated around singularities, creating what we refer to as *graded h-refinement*. The idea of graded meshes is not new; it has been proven to be a powerful tool for local a priori refinement of finite elements towards corner singularities [24–27]. More recently, a similar concept has been proposed for IGA in a multi-patch context, but the isogeometric parameterization is assumed to be smooth, at least in the points towards which the mesh is locally refined [28,49]. However, this requirement is not satisfied by the single-patch parameterization $\boldsymbol{F}$ that we employ in this paper.

We begin with a detailed description of the standard uniform refinement procedure for single-patch circular sectors and subsequently introduce the proposed modification to achieve graded h-refinement. As a starting point, we recall the coarse parametric and physical Bézier meshes (4.2) and (4.3), respectively, both of which are illustrated in Fig. 5. It is crucial to ensure that the parameterization $\boldsymbol{F}$ and the weight function W remain unchanged during refinement. This can be done in practice by bisecting each interval of the coarse mesh a certain number of times. For instance, let $J_1, J_2 \in \mathbb{N}$ such that $J_2/4 \in \mathbb{N}$ and define $h_1 := \frac{1}{J_1}$ and $h_2 := \frac{1}{J_2}$. Then, the knot vectors

$$\Xi_1^{h_1} = \left\{0, 0, \frac{1}{J_1}, \frac{2}{J_1}, \dots, \frac{J_1 - 1}{J_1}, 1, 1\right\}, \tag{4.5}$$

$$\Xi_2^{h_2} = \left\{0, 0, 0, \frac{1}{J_2}, \frac{2}{J_2}, \dots, \frac{J_2/4 - 1}{J_2}, \frac{J_2/4}{J_2}, \frac{J_2/4}{J_2}, \frac{J_2/4 + 1}{J_2}, \frac{J_2/4 + 2}{J_2}, \dots, \frac{J_2/2 - 1}{J_2}, \frac{J_2/2}{J_2}, \frac{J_2/2}{J_2}, \dots, 1, 1, 1\right\}$$

are uniform refinements of the coarse knot vectors Ξ_1^0 and Ξ_2^0, respectively. The vectors of knots without repetitions are simply given by

$$\begin{aligned} Z_1^{h_1} &= \left\{0, \frac{1}{J_1}, \frac{2}{J_1}, \dots, \frac{J_1 - 1}{J_1}, 1\right\} \\ &= \{\zeta_{1,j_1} := (j_1 - 1)h_1 : 1 \le j_1 \le J_1 + 1\}, \\ Z_2^{h_2} &= \left\{0, \frac{1}{J_2}, \frac{2}{J_2}, \dots, \frac{J_2 - 1}{J_2}, 1\right\} \\ &= \{\zeta_{2,j_2} := (j_2 - 1)h_2 : 1 \le j_2 \le J_2 + 1\}. \end{aligned}$$

We obtain the refined parametric Bézier mesh

$$\widehat{\mathcal{M}} = \left\{Q_j \subset \hat{\Omega} : Q_j = Q_{(j_1,j_2)} = \left(\zeta_{1,j_1}, \zeta_{1,j_1+1}\right) \times \left(\zeta_{2,j_2}, \zeta_{2,j_2+1}\right), \boldsymbol{j} \in \boldsymbol{J}\right\} \tag{4.6}$$

with $\boldsymbol{J} := \{\boldsymbol{j} = (j_1, j_2) : 1 \le j_1 \le J_1, 1 \le j_2 \le J_2\}$. Each element of the coarse mesh $\widehat{\mathcal{M}}_0$, given by (4.2), is uniformly split up J_1 times in ζ_1-direction and $J_2/4$ times in ζ_2-direction. The same effect holds for the refined physical Bézier mesh

$$\mathcal{M} = \{K_j \subset \Omega : K_j = \boldsymbol{F}(Q_j), \boldsymbol{j} \in \boldsymbol{J}\}.$$

In total, the resulting meshes contain $J_1 \cdot J_2$ uniformly refined elements. An exemplary illustration of such parametric and physical meshes after uniform refinement with $J_1 = 6$ and $J_2 = 16$ is presented in Fig. 6a.

Now, our objective is to adjust the refinement process to achieve a physical Bézier mesh that is locally refined around the conical point of the circular sector. When the isogeometric mapping $\boldsymbol{F}$ is applied to the closure of the parametric domain, the singular edge $\{(0, \zeta_2) : \zeta_2 \in [0, 1]\}$ is mapped onto the singular point $\boldsymbol{S} = (0, 0)$. Hence, we need to grade the knots in the parametric domain towards the singular edge to obtain a finer mesh in the physical domain locally near the singularity. To this end, we introduce a *grading parameter* $\mu \in (0, 1]$ and modify the knot insertion process in ζ_1-direction. Instead of the vector (4.5), we use the graded knot vector

$$\Xi_1^{h_1,\mu} = \{0, 0, (h_1)^{\frac{1}{\mu}}, (2h_1)^{\frac{1}{\mu}}, \dots, ((J_1 - 1)h_1)^{\frac{1}{\mu}}, 1, 1\} \tag{4.7}$$

The graded vector of knots without repetitions is then given by

$$Z_1^{h_1,\mu} = \{\zeta_{1,j_1}^\mu := \left((j_1 - 1)h_1\right)^{\frac{1}{\mu}} : 1 \le j_1 \le J_1 + 1\}. \tag{4.8}$$

Note that the choice $\mu = 1$ leads to uniform refinement. Thus, the graded refinement scheme is a generalization of the uniform version. In ζ_2-direction, no adjustments are needed, and we employ the same knot vector $\Xi_2^{h_2}$ and vector of breakpoints $Z_2^{h_2}$ as in the uniform refinement

procedure. By combining the two directions, we obtain the graded parametric mesh

$$\widehat{\mathcal{M}}^\mu = \left\{ Q_j^\mu \subset \widehat{\Omega} : Q_j^\mu = Q^\mu_{(j_1,j_2)} = \left(\zeta^\mu_{1,j_1}, \zeta^\mu_{1,j_1+1}\right) \times \left(\zeta_{2,j_2}, \zeta_{2,j_2+1}\right), \; j \in \boldsymbol{J} \right\}$$

which is locally refined towards the singular edge. The corresponding physical Bézier mesh

$$\mathcal{M}^\mu = \left\{ K_j^\mu \subset \Omega : K_j^\mu = \boldsymbol{F}(Q_j^\mu), j \in \boldsymbol{J} \right\}$$

is locally refined towards the conical point of the circular sector. In Fig. 6b, we illustrate this effect by depicting the graded parametric and physical Bézier meshes after refining with $J_1 = 6$ and $J_2 = 16$ and a grading parameter of $\mu = 1/2$.

4.4.2. Anisotropic elements in the graded meshes

Both the graded parametric and physical Bézier meshes contain anisotropic elements. The aspect ratio of the rectangular parametric elements $Q_j \in \widehat{\mathcal{M}}^\mu$ close to the singular edge of $\widehat{\Omega}$ is given by

$$\frac{h_2}{h_1^{1/\mu}} = C h^{1-\frac{1}{\mu}} \to \infty \quad \text{for } h_1 = h_2 = h \to 0 \text{ and } \mu < 1\,. \tag{4.9}$$

Thus, the elements are highly stretched in ζ_2-direction. This effect is fully induced by the mesh grading and depends on the grading parameter μ. For $\mu = 1$ and $\frac{1}{C} h_2 \le h_1 \le C h_2$, that is, for evenly uniform refinement in both directions, the aspect ratio (4.9) is constant and the mesh is isotropic.

In contrast, the latter does not hold for the physical Bézier mesh. We compute the aspect ratio of the elements $K_j \in \mathcal{M}^\mu$ close to the singular point $\boldsymbol{S}$ using the lengths of their largest edges,

$$\frac{h_1^{1/\mu}}{h_1^{1/\mu} h_2} = \frac{1}{h} \to \infty \quad \text{for } h_1 = h_2 = h \to 0\,. \tag{4.10}$$

The elements are highly stretched in radial direction, corresponding to the ζ_1-direction in the parametric domain. Hence, the stretching direction is reversed from the parametric to the physical mesh. Moreover, the physical mesh elements are anisotropic regardless of the mesh grading as the aspect ratio (4.10) does not depend on the grading parameter μ. Consequently, the anisotropy in the physical mesh is exclusively induced by the singular parameterization $\boldsymbol{F}$. In Section 5.4, we explore a slight modification of our refinement approach to avoid this effect.

4.4.3. Choice of the grading parameter

It remains to be discussed how to choose the grading parameter μ such that optimal convergence orders for the singular solutions and corresponding eigenvalues are achieved. Here, we capitalize on existing knowledge about graded finite element meshes. While there is extensive literature on this topic, we only list a few important works here [24–27,52].

According to the results from Section 2.3, the strongest singularity that Laplace eigenfunctions of circular sectors can possibly have is of type r^{ν_1} with $\nu_1 = \frac{\pi}{\omega} \ge \frac{1}{2}$. Therefore, if we consider an arbitrary eigenfunction $u = u_{\nu_k,m}$, where $k \in \mathbb{N}_0$ and $m \in \mathbb{N}$ are not known a priori, we can only expect that $u \in H^s(\Omega)$ for all $s < \nu_1 + 1$. If we restrict ourselves to classical Sobolev spaces, we can assume no more than $u \in H^1(\Omega)$ for circular sectors with angles $\omega > \pi$. Besides, it has been shown that the convergence of the discrete eigenvalues can be described in terms of the $H^1(\Omega)$-error of the corresponding Galerkin approximations of the eigenfunctions [3,53,54]. Hence, we incorporate a grading parameter that has been proven effective to achieve optimal convergence of the $H^1(\Omega)$-error, which is of order p for finite elements of degree p. The required conditions are [52]

$$\mu < \frac{\nu_1}{p} \quad \text{and} \quad \mu \le 1\,. \tag{4.11}$$

We transfer these conditions to IGA for NURBS of degree $\boldsymbol{p} = (p_1, p_2)$ with $p = \min(p_1, p_2)$. However, there is still some freedom how to precisely choose μ for a numerical computation and several guidelines have been discussed in the literature, see for instance [52]. Our experience, which we share in the numerical Examples 5.3 and 5.9, has shown that

$$\mu = 0.9 \cdot \frac{\nu_1}{p} \tag{4.12}$$

is a good choice, provided that $\frac{\nu_1}{p} < 1$.

In general, it is crucial to be aware of varying regularity properties of the Laplace eigenmodes of circular sectors. Eigenfunctions of low regularity are approximated more accurately by graded meshes due to the optimal convergence which is not achieved by uniform meshes. In contrast, smooth eigenfunctions are actually approximated better by uniform meshes. Unnecessary grading of the mesh has a negative effect on the approximation constant, although the optimal convergence rate is not affected. We will demonstrate this behavior later in the numerical examples. Of course, the choice of the grading parameter also depends on the degree of the basis functions and the objective of the computation. If the goal is to approximate a specific eigenfunction $u = u_{\nu_k,m}$ for a given $k \in \mathbb{N}_0$ and $m \in \mathbb{N}$, it is better to choose

$$\mu = \begin{cases} 1 & \text{if } \nu_k \in \mathbb{N}_0 \text{ or } \nu_k \ge p\,, \\ 0.9 \cdot \dfrac{\nu_k}{p} & \text{else}\,, \end{cases} \tag{4.13}$$

where we recall the regularity results of Lemma 2.2 and Lemma 2.3. If multiple eigenfunctions have to be approximated at once with a guaranteed overall accuracy, the strongest grading parameter (4.12) should be chosen. In contrast, if poor approximations of the few eigenfunctions of very low regularity are not considered problematic, it may be advisable to use uniform meshes. To gain a better understanding, all the described effects of mesh grading will be illustrated numerically in the next section.

5. Numerical results

Finally, we perform some numerical tests showing the efficiency of our proposed approach to approximate the Laplace eigenvalue problem on circular sectors (2.1). First, we illustrate optimal convergence orders for the eigenpairs with respect to graded h-refinement for appropriately chosen grading parameters. In a second experiment, we demonstrate the advantages of our method for the computation of multiple eigenvalues, where we further examine spectral approximation properties of maximally smooth spline spaces on circular sectors. Finally, we combine our method with a hierarchical approach to avoid anisotropic elements in the physical Bézier mesh and save unnecessary degrees of freedom. In accordance with the main parts of the paper, we provide numerical results for the most complex circular sector with an inner angle of 2π, which serves as a prototype for smaller angles.

All numerical experiments are carried out using the Matlab computing package GeoPDEs 3.2.2 [55,56] where the graded h-refinement algorithm can be implemented easily by adapting one line of the standard knot refining routine *kntrefine* that is provided in the package.

Moreover, all integrals are computed using a Gauss-Legendre quadrature rule with 36 quadrature points per mesh element. In more detail, 6 quadrature points are employed in both univariate directions, such that the bilinear forms defined in Section 2.5 are computed exactly for tensor product polynomials in the parametric domain up to degree $p = 5$. The $H^1(\Omega)$-errors of the eigenfunctions are evaluated using the same quadrature formula.

All convergence plots are presented with respect to the total number of degrees of freedom ndof, and not the mesh parameter h. Since the meshes are constructed by a tensor product approach, $\text{ndof} \approx h^{-2}$ holds. Thus, if the expected convergence rate w.r.t the mesh size is $\mathcal{O}(h^q)$, the corresponding rate w.r.t. to ndof can be described by $\text{ndof}^{-q/2}$. However, since we are only talking about convergence rates w.r.t to the mesh size

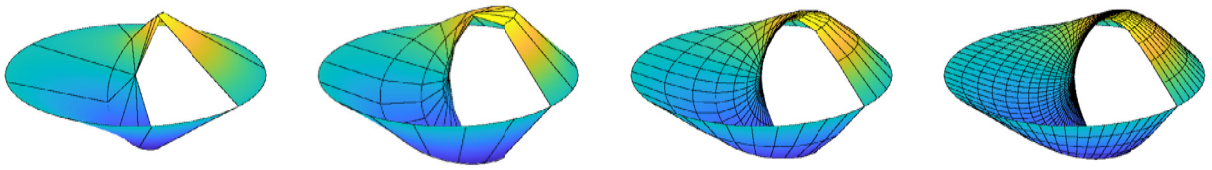

Fig. 7. Approximation of the eigenfunction $u_{\nu_1,1}$ using NURBS of lowest possible degree $\boldsymbol{p}=(p_1,p_2)=(1,2)$ and regularity $\boldsymbol{k}=(0,1)$ while gradually refining $J_1=\frac{J_2}{4}=2,4,8,16$ times with grading parameter $\mu=0.9\cdot\frac{\nu_1}{p_1}=0.45$, recall (4.11).

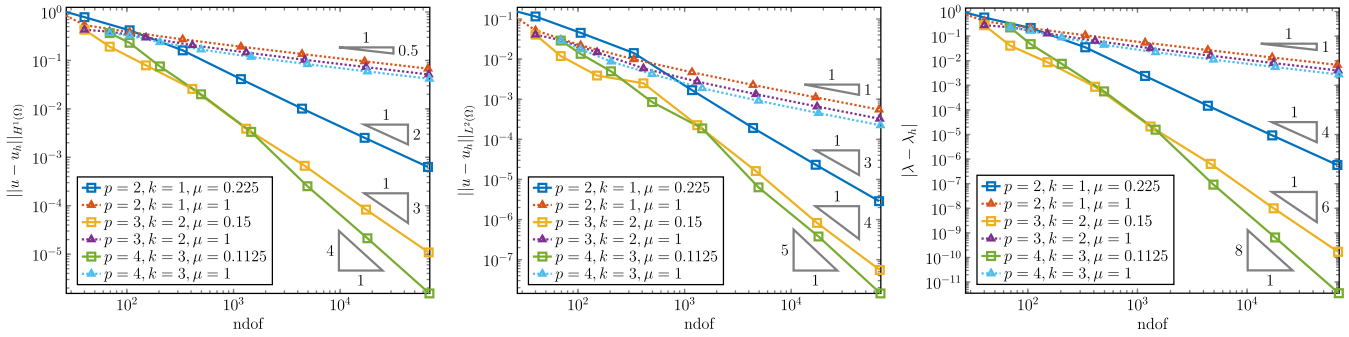

Fig. 8. Approximation errors for the eigenfunction $u=u_{\nu_1,1}$ and its corresponding eigenvalue $\lambda=\lambda_{\nu_1,1}$ using gradually and uniformly refined NURBS of degree $\boldsymbol{p}=(p,p)$, $p\in\{2,3,4\}$, and regularity $\boldsymbol{k}=(p-1,p-1)$. We set $\mu=0.9\frac{\nu_1}{p}=\frac{0.9}{2p}$ for graded meshes and $\mu=1$ corresponds to uniform refinement.

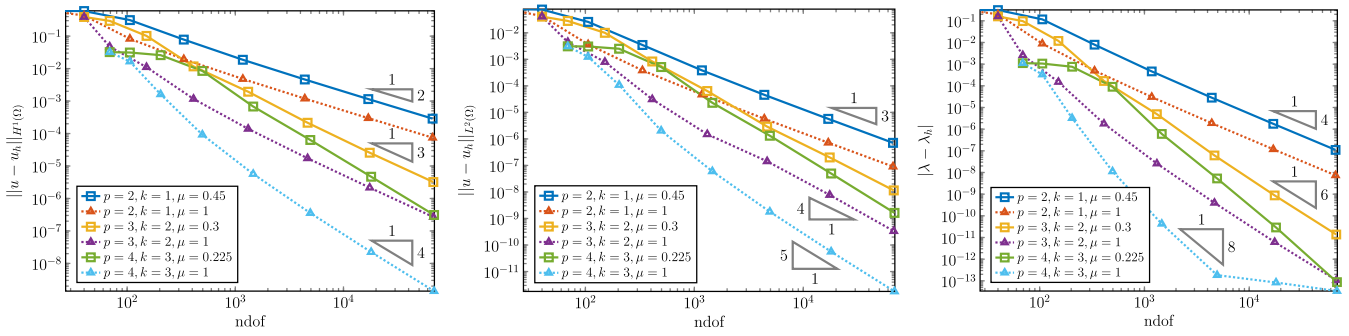

Fig. 9. Approximation errors for the eigenfunction $u=u_{\nu_2,1}$ and its corresponding eigenvalue $\lambda=\lambda_{\nu_2,1}$ using gradually and uniformly refined NURBS of degree $\boldsymbol{p}=(p,p)$, $p\in\{2,3,4\}$, and regularity $\boldsymbol{k}=(p-1,p-1)$. We set $\mu=0.9\frac{\nu_2}{p}=\frac{0.9}{p}$ for graded meshes and $\mu=1$ corresponds to uniform refinement.

in our manuscript, the experimental orders of convergence displayed in all error plots and tables are those w.r.t to h.

5.1. Optimal convergence to the analytical eigenfunctions and eigenvalues

In the first examples, we show that our method produces optimal convergence rates for the approximation of the Laplace eigenpairs of circulars sectors. As discussed in Section 2.4, the sequence of eigenmodes consists of both singular and smooth functions which are referred to as eigenfunctions of type (A) and type (B), respectively. We exemplarily pick one eigenfunction out of each group and evaluate the resulting approximation errors.

Example 5.1 *(Eigenfunction of type (A)).* We approximate the eigenvalue $\lambda_{\nu_1,1}$ of the unit disk with crack and its corresponding eigenfunction $u_{\nu_1,1}$, which has the strongest possible singularity of type r^{ν_1}, where $\nu_1=1/2$. In Fig. 7, we illustrate the discrete eigenfunction throughout the gradual refinement process using NURBS of the lowest possible degree $\boldsymbol{p}=(1,2)$ and regularity $\boldsymbol{k}=(0,1)$. The solution is showcased for various graded mesh refinements, ranging from relatively coarse to further refined ones. Fig. 8 presents the $H^1(\Omega)$- and $L^2(\Omega)$-error of the eigenfunction and the absolute eigenvalue error using NURBS of polynomial degree $\boldsymbol{p}=(p,p)$, $p\in\{2,3,4\}$, and regularity $\boldsymbol{k}=(p-1,p-1)$ with varying grading parameters μ. Precisely, we set $\mu=1$ for uniform and $\mu=0.9\cdot\nu_1/p$ for graded refinement, as proposed in formula (4.12). On uniform meshes, the convergence rate with respect to the $H^1(\Omega)$- and $L^2(\Omega)$-error of the eigenfunction is $1/2$ and 1, respectively, for all $\boldsymbol{p}$. In contrast, graded meshes yield optimal convergence orders p and $p+1$, respectively. Consequently, the discrete eigenvalue converges to the exact one with order 1 for any $\boldsymbol{p}$ during uniform refinement, whereas mesh grading recovers the optimal convergence rate of $2p$.

Example 5.2 *(Eigenfunction of type (B)).* Next, we approximate the eigenvalue $\lambda_{\nu_2,1}$ of the unit disk with crack and its corresponding eigenfunction $u=u_{\nu_2,1}$, where $\nu_2=1$. As shown in Lemma 2.3, this is a smooth function. Fig. 9 depicts the $H^1(\Omega)$- and $L^2(\Omega)$-error of the eigenfunction and the absolute eigenvalue error using NURBS of polynomial degree $\boldsymbol{p}=(p,p)$, $p\in\{2,3,4\}$, and regularity $\boldsymbol{k}=(p-1,p-1)$ with different grading parameters μ. Here, the convergence orders with uniform and graded refinement are equal, but the approximation constant of the uniform meshes is superior. This result justifies the recommended grading parameter (4.13) if a specific eigenfunction is approximated.

5.2. Optimal grading parameter

In this section, we validate the recommended grading parameter (4.12). Since we already know from Example 5.2 that graded meshes

Table 2
Approximation errors $\|u-u_h\|_{H^1(\Omega)}$ (and corresponding experimental orders of convergence) for the eigenfunction $u=u_{\nu_1,1}$ using gradually refined NURBS of degree $\boldsymbol{p}=(2,2)$ and regularity $\boldsymbol{k}=(1,1)$ with different grading parameters μ.

ndof	$\mu=0.7\frac{\nu_1}{p}=0.175$	$\mu=0.9\frac{\nu_1}{p}=0.225$	$\mu=1.1\frac{\nu_1}{p}=0.275$	$\mu=1.3\frac{\nu_1}{p}=0.325$
19	1.2500e + 00	1.2500e + 00	1.2500e + 00	1.2500e + 00
40	8.4778e − 01 (1.18)	7.8366e − 01 (1.42)	7.3268e − 01 (1.63)	6.9185e − 01 (1.81)
106	5.3217e − 01 (1.05)	4.1982e − 01 (1.41)	3.4478e − 01 (1.70)	2.9860e − 01 (1.90)
334	2.3431e − 01 (1.52)	1.6133e − 01 (1.78)	1.1590e − 01 (2.02)	9.1099e − 02 (2.20)
1174	6.6457e − 02 (2.08)	4.1166e − 02 (2.26)	2.9150e − 02 (2.28)	2.4590e − 02 (2.16)
4390	1.6234e − 02 (2.18)	1.0125e − 02 (2.17)	7.4213e − 03 (2.12)	7.0980e − 03 (1.92)
16966	4.0166e − 03 (2.09)	2.5243e − 03 (2.08)	1.9224e − 03 (2.02)	2.1679e − 03 (1.77)
66694	1.0014e − 03 (2.04)	6.3171e − 04 (2.04)	5.0293e − 04 (1.97)	6.9175e − 04 (1.68)
264454	2.5016e − 04 (2.02)	1.5817e − 04 (2.02)	1.3267e − 04 (1.94)	2.2764e − 04 (1.62)

Table 3
Approximation errors $|\lambda-\lambda_h|$ (and corresponding experimental orders of convergence) for the eigenvalue $\lambda=\lambda_{\nu_1,1}$ using gradually refined NURBS of degree $\boldsymbol{p}=(2,2)$ and regularity $\boldsymbol{k}=(1,1)$ with different grading parameters μ.

ndof	$\mu=0.7\frac{\nu_1}{p}=0.175$	$\mu=0.9\frac{\nu_1}{p}=0.225$	$\mu=1.1\frac{\nu_1}{p}=0.275$	$\mu=1.3\frac{\nu_1}{p}=0.325$
19	1.3869e + 00	1.3869e + 00	1.3869e + 00	1.3869e + 00
40	6.4991e − 01 (2.31)	5.7113e − 01 (2.71)	5.1477e − 01 (3.02)	4.7780e − 01 (3.25)
106	2.9613e − 01 (1.78)	2.1387e − 01 (2.22)	1.5767e − 01 (2.67)	1.2036e − 01 (3.12)
334	7.2689e − 02 (2.61)	3.5189e − 02 (3.35)	1.8634e − 02 (3.96)	1.1722e − 02 (4.32)
1174	6.2156e − 03 (4.06)	2.4139e − 03 (4.43)	1.2198e − 03 (4.50)	8.7535e − 04 (4.29)
4390	3.7938e − 04 (4.33)	1.4801e − 04 (4.32)	7.9694e − 05 (4.22)	7.3365e − 05 (3.84)
16966	2.3343e − 05 (4.17)	9.2259e − 06 (4.15)	5.3569e − 06 (4.04)	6.8598e − 06 (3.54)
66694	1.4526e − 06 (4.08)	5.7818e − 07 (4.07)	3.6684e − 07 (3.94)	6.9934e − 07 (3.35)
264454	9.0687e − 08 (4.04)	3.6253e − 08 (4.03)	2.5533e − 08 (3.88)	7.5794e − 08 (3.24)

Table 4
Approximation errors $\|u-u_h\|_{H^1(\Omega)}$ (and corresponding experimental orders of convergence) for the eigenfunction $u=u_{\nu_1,1}$ using gradually refined NURBS of degree $\boldsymbol{p}=(2,2)$ and regularity $\boldsymbol{k}=(0,0)$ with different grading parameters μ.

ndof	$\mu=0.7\frac{\nu_1}{p}=0.175$	$\mu=0.9\frac{\nu_1}{p}=0.225$	$\mu=1.1\frac{\nu_1}{p}=0.275$	$\mu=1.3\frac{\nu_1}{p}=0.325$
19	1.2500e + 00	1.2500e + 00	1.2500e + 00	1.2500e + 00
69	8.4272e − 01 (0.69)	7.7901e − 01 (0.82)	7.2859e − 01 (0.94)	6.8807e − 01 (1.04)
265	5.0853e − 01 (0.81)	3.8736e − 01 (1.12)	3.1956e − 01 (1.32)	2.7379e − 01 (1.47)
1041	2.0838e − 01 (1.36)	1.4368e − 01 (1.51)	1.0577e − 01 (1.68)	8.5486e − 02 (1.77)
4129	6.1687e − 02 (1.81)	3.9273e − 02 (1.92)	2.8324e − 02 (1.95)	2.4196e − 02 (1.87)
16449	1.5879e − 02 (1.99)	9.9994e − 03 (2.00)	7.3687e − 03 (1.97)	7.0632e − 03 (1.80)
65665	3.9938e − 03 (2.01)	2.5163e − 03 (2.00)	1.9187e − 03 (1.95)	2.1609e − 03 (1.72)
262401	9.9992e − 04 (2.00)	6.3120e − 04 (2.00)	5.0257e − 04 (1.94)	6.8945e − 04 (1.65)

Table 5
Approximation errors $|\lambda-\lambda_h|$ (and corresponding experimental orders of convergence) for the eigenvalue $\lambda=\lambda_{\nu_1,1}$ using gradually refined NURBS of degree $\boldsymbol{p}=(2,2)$ and regularity $\boldsymbol{k}=(0,0)$ with different grading parameters μ.

ndof	$\mu=0.7\frac{\nu_1}{p}=0.175$	$\mu=0.9\frac{\nu_1}{p}=0.225$	$\mu=1.1\frac{\nu_1}{p}=0.275$	$\mu=1.3\frac{\nu_1}{p}=0.325$
19	1.3869e + 00	1.3869e + 00	1.3869e + 00	1.3869e + 00
69	6.4264e − 01 (1.34)	5.6592e − 01 (1.56)	5.1135e − 01 (1.74)	4.7551e − 01 (1.87)
265	2.8072e − 01 (1.32)	1.9449e − 01 (1.71)	1.3751e − 01 (2.10)	1.0247e − 01 (2.45)
1041	5.8947e − 02 (2.38)	2.8602e − 02 (2.92)	1.5714e − 02 (3.30)	1.0398e − 02 (3.48)
4129	5.3909e − 03 (3.55)	2.2029e − 03 (3.80)	1.1530e − 03 (3.87)	8.4806e − 04 (3.72)
16449	3.6315e − 04 (3.95)	1.4437e − 04 (3.99)	7.8573e − 05 (3.93)	7.2659e − 05 (3.59)
65665	2.3079e − 05 (4.00)	9.1678e − 06 (4.01)	5.3367e − 06 (3.91)	6.8164e − 06 (3.44)
262401	1.4484e − 06 (4.01)	5.7725e − 07 (4.00)	3.6631e − 07 (3.88)	6.9483e − 07 (3.31)

are not required for the approximation of eigenfunctions of type (B), we solely conduct a numerical investigation with respect to the optimal grading parameter for an eigenfunction of type (A), recall formula (4.13).

Example 5.3. We approximate the eigenvalue $\lambda_{\nu_1,1}$ of the unit disk with crack and its corresponding eigenfunction $u_{\nu_1,1}$, which has the strongest possible singularity of type r^{ν_1} with $\nu_1=1/2$, this time using gradually refined NURBS of degree $\boldsymbol{p}=(2,2)$ and regularity $\boldsymbol{k}=(1,1)$ with different grading parameters μ. In Tables 2 and 3, we list the $H^1(\Omega)$-errors of the eigenfunction and the absolute eigenvalue errors, respectively, together with the corresponding experimental convergence rates. We observe suboptimal convergence orders for grading parameters $\mu>\frac{\nu_1}{p}$ and optimal rates for $\mu<\frac{\nu_1}{p}$ as stated in condition (4.11). Among the two sufficiently graded meshes, the moderate grading for $\mu=0.9\frac{\nu_1}{p}$ is preferable over the strong mesh grading with $\mu=0.7\frac{\nu_1}{p}$ due to an improved approximation constant. These observations explain our recommendation (4.12). For C^0-continuous splines, we observe a similar behavior. In Tables 4 and 5, we show the $H^1(\Omega)$-errors of the eigen-

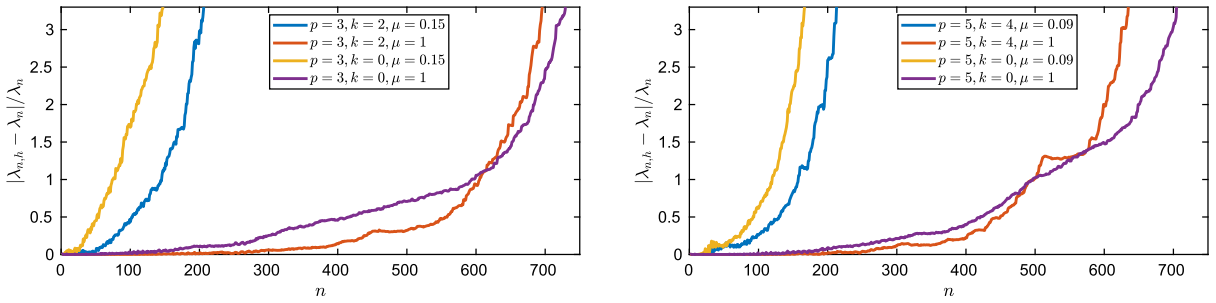

Fig. 10. Relative eigenvalue errors, ordered by discrete eigenvalue size, using gradually and uniformly refined NURBS of degree $\boldsymbol{p} = (p, p)$ and regularity $\boldsymbol{k} = (k, k)$. A total of 916 degrees of freedom is used in all the computations. We set $\mu = 0.9\frac{\nu_1}{p} = \frac{0.9}{2p}$ for graded meshes and $\mu = 1$ corresponds to uniform refinement.

function and the absolute eigenvalue errors, respectively, together with the corresponding experimental convergence rates for NURBS of degree $\boldsymbol{p} = (2, 2)$ and regularity $\boldsymbol{k} = (0, 0)$. Again, we see that the choice $\mu = 0.9\frac{\nu_1}{p}$ leads to the best approximation constant while guaranteeing optimal convergence rates. Moreover, a comparison of Tables 2 and 4 indicates that the approximation constant regarding the $H^1(\Omega)$-error of the eigenfunction is about four times smaller for for smooth splines than for C^0-continuous splines, while approximately the same number of degrees of freedom is employed. Hence, smooth splines lead to a better convergence on a per-degree-of freedom basis than their C^0-continuous counterparts.

5.3. Spectral approximation properties of smooth splines on circular sectors

Naturally, the solution of an eigenvalue problem is not just given by single eigenvalues and eigenfunctions but by an infinite sequence of such. Therefore, we use our approach to compute multiple solutions of the model problem (2.1) in the next numerical experiment. The different regularity properties of the exact Laplace eigenfunctions, outlined in Section 2.3, will be crucial to understand the numerical results.

In this context, it is of interest whether some of the spectral approximation properties of smooth splines, which have been shown for rectangular domains in the literature [9,12,14,15] can be extended to circular sectors. In most of the related works, the full discrete spectrum is approximated, that is, one discrete eigenvalue is computed per computational degree of freedom. The power of smooth splines in this setting is twofold. First, finite elements produce so called spectral branches, i.e., the eigenvalue error jumps for higher frequencies, a phenomenon which does not occur with maximally smooth splines. Second, the overall approximation constant of smooth splines is better over the whole discrete spectrum. In the following, we conduct numerical studies to investigate comparable properties of the discrete spectrum of circular sectors.

At this point, smooth splines on circular sectors should be considered cautiously. In ζ_2-direction, the geometry mapping $\boldsymbol{F}$ is based on the classical quadratic NURBS parameterizations of circles. Typically, circles are constructed from multiple arcs smaller than 180°, and the resulting bases are no more than C^0-continuous at the junctions of the arcs [9, Chapter 2.4.1.1]. In particular, we use four arcs of 90° for the discretization of the unit disk with crack. Therefore, the univariate NURBS basis functions in ζ_2-direction are only C^0-continuous at the points $\{1/4, 1/2, 3/4\}$. We explicitly compute these functions in Appendix A. Consequently, the coarse tensor product basis functions (4.4) are C^0-continuous along the lines $\{(r\cos\varphi, r\sin\varphi) : r \in (0, 1), \varphi \in \{\pi/2, \pi, 3\pi/2\}\}$. After refinement, these C^0-lines will still be present. However, this is considered a minor limitation for the smoothness of the NURBS basis functions since, in all the regions between the specified lines of C^0-continuity, the regularity can be increased as desired by using the k-refinement algorithm introduced in Section 3.1.

Example 5.4. We compute the full discrete spectrum of the unit disk with crack using different parameters, all of which result in systems with a total of 916 degrees of freedom. We compare bicubic C^2-continuous NURBS and biquintic C^4-continuous NURBS on uniform and graded meshes with their C^0-continuous counterparts. As outlined in Section 4.4.3, we choose the strong grading parameter $\mu = 0.9 \cdot \nu_1/p$ from (4.12) for the graded meshes since we want to compute all discrete eigenvalues at once and some of them have corresponding eigenfunctions with the strong singularity of type r^{ν_1}. Fig. 10 presents the relative eigenvalue errors, ordered by the discrete eigenvalue size. For both types of mesh, it becomes evident that the approximation accuracy of the displayed spectrum increases with higher NURBS regularity, except for the very upper part of the spectrum. Hence, the positive findings concerning the approximation constant of smooth splines, which have been illustrated in the literature for rectangular domains, can be extended to the case of circular sectors, at least in the lower part of the spectrum. However, we cannot identify the appearance of spectral branches. Our results on uniform meshes optically resemble those in [57], where the Laplace-Beltrami eigenvalue problem has been considered on the unit sphere. In general, higher eigenvalues are approximated better by uniform meshes, which is attributable to their superior approximation constant on coarse refinement levels, as it can also be observed in Example 5.1 and 5.2.

Remark 5.5. In Example 5.4 and Fig. 10, each discrete eigenvalue is associated to an exact eigenvalue by ordering both sequences in ascending order. However, this matching is not always correct, that is, a discrete eigenvalue $\lambda_{n,h}$ might be an approximation of the exact eigenvalue λ_m with $n \neq m$. Techniques for a proper association of discrete and exact eigenvalues have been proposed in the literature, but it has also been observed that the impact of mismatching is marginal [8,14,15,58].

To demonstrate the strength of our proposed graded refinement approach, we need to adopt a slightly different point of view. The primary benefit of gradually refined NURBS is the optimal approximation of eigenfunctions with low regularity and their corresponding eigenvalues. This property is asymptotic which only comes into effect for an increasing number of computational degrees of freedom. Therefore, we decide to compute a fixed number of discrete eigenvalues and increase the number of degrees of freedom. Since our objective is to approximate the eigenvalues of circular sectors in the best possible way and the accuracy of Galerkin methods generally decreases for higher frequencies [59, Chapter 6.3], it is natural to consider only the lower discrete eigenvalues and refine the mesh. The analysis of spectral branches up to the highest discrete frequencies is of specific interest for related time-dependent problems in explicit numerical schemes as the critical time-step size calculation is inversely proportional to the maximum discrete eigenfrequency [60], but we do not consider this here.

Example 5.6. We compare the relative errors for the 100 smallest Laplace eigenvalues of the unit disk with crack using suitably graded and uniform meshes. Again, we choose the strong grading parameter $\mu = 0.9 \cdot \nu_1/p$ from (4.12) since we want to approximate multiple eigenvalues at once with a guaranteed optimal convergence rate.

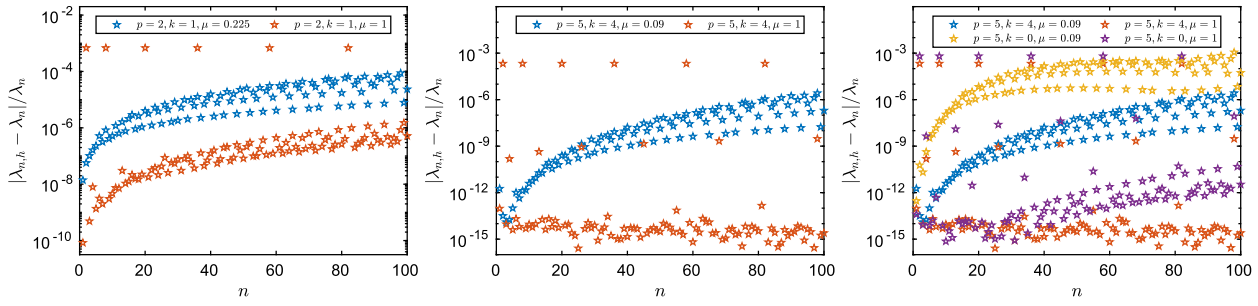

Fig. 11. Relative errors for the first 100 eigenvalues, ordered by discrete eigenvalue size, using gradually and uniformly refined NURBS of degree $\boldsymbol{p}=(p,p)$ and regularity $\boldsymbol{k}=(k,k)$. In total, 67731 degrees of freedom are used in all the computations. We set $\mu=0.9\frac{\nu_1}{p}=\frac{0.9}{2p}$ for graded meshes and $\mu=1$ corresponds to uniform refinement.

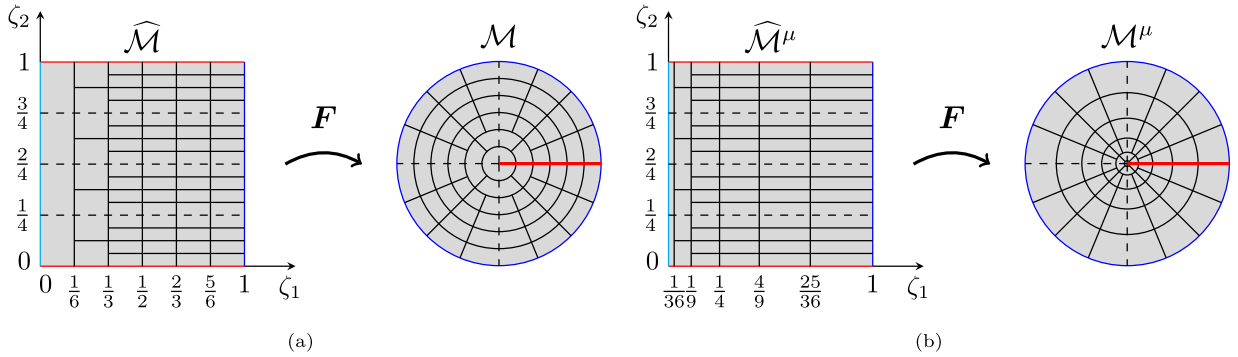

Fig. 12. Hierarchical parametric and physical Bézier meshes $\widehat{\mathcal{M}}$ and $\mathcal{M}$ after refining with $J_1=6$ and $J_2=16$. Solid black lines are used for new subdivisions and dashed black lines for the initial coarse meshes $\widehat{\mathcal{M}}_0$ and $\mathcal{M}_0$. Note the difference to the tensor product meshes in Fig. 6. (a) Uniform refinement. (b) Graded refinement with grading parameter $\mu=\frac{1}{2}$.

First, we employ biquadratic, C^1-continuous NURBS in a system with 67731 degrees of freedom, which arises for 128 subdivisions of the coarse mesh in each parametric direction as discussed in Section 4. The results are presented in the left hand plot of Fig. 11. The uniform mesh produces some very poor approximations along with many accurate ones. More precisely, the approximates of the eigenvalues $\lambda_2,\lambda_8,\lambda_{20},\dots$ are significantly less accurate compared to the rest. In Table 1, we can see that these are the eigenvalues that belong to eigenfunctions of the lowest possible regularity. As outlined in Example 5.1, uniformly refined approximations do not converge optimally. Hence, these eigenvalues produce outliers in the spectral approximation since the remaining eigenvalues are associated with eigenfunctions of higher regularity which are also approached accurately on uniform meshes. In contrast, the eigenvalue errors achieved by the graded mesh are evenly distributed. All the eigenvalues are approximated with a comparable accuracy, which is naturally decreasing for higher eigenvalues. In particular, the outliers of the uniform version, $\lambda_2,\lambda_8,\lambda_{20},\dots$, are approximated much better on the graded mesh. However, the graded approximation of the remaining eigenvalues with corresponding eigenfunctions of higher regularity is worse than the uniform variant. For this type of eigenvalues, the grading is unnecessary and has a negative effect on the approximation constant, as discussed in Section 4.4.3 and Example 5.2.

In a second test, we employ biquintic, C^4-continuous NURBS in a system with 67731 degrees of freedom on a uniform and graded mesh. The relative eigenvalue errors are depicted in the middle plot of Fig. 11. Here, in addition to the poor approximations of $\lambda_2,\lambda_8,\lambda_{20},\dots$, the uniform mesh produces a second group of outliers, given by the eigenvalues $\lambda_4,\lambda_{13},\lambda_{26},\dots$. In Table 1, we observe that these eigenvalues belong to eigenfunctions with the second strongest singularity. Due to the high degree of the NURBS, the difference between optimal and reduced convergence rates also becomes noticeable for this group of eigenvalues. Contrarily, the graded mesh produces an evenly distributed error point cloud, but less accurate results for eigenvalues that correspond to smoother eigenfunctions.

Lastly, we compare biquintic C^4-continuous NURBS with their C^0-continuous counterparts on uniform and graded meshes. The results are presented in the right hand plot of Fig. 11. For both types of mesh, the approximation is more accurate with smooth splines, although the same number of degrees of freedom is used. The superiority of smooth splines is even clearer on graded meshes as they do not produce outliers. Hence, we can again confirm the excellent spectral approximation constant of smooth splines on circular sectors. Since we consider only the very lower part of the spectrum here, which can not be analyzed in the study conducted in Fig. 10, this series of results complements the previous findings of Example 5.4.

In summary, the two numerical examples of this section show that the combination of single-patch mesh grading with maximally smooth splines on circular sectors is a very powerful approach to approximate the Laplace eigenvalues of circular sectors. It is computationally cheap, accurate and produces an evenly distributed error throughout the considered eigenvalues.

5.4. Hierarchical meshes in combination with graded refinement

Finally, we present a variation of our method that aims at improving the constructed graded meshes. As discussed in Section 4.4.2, the physical Bézier mesh is anisotropic next to the conical point of the circular sector due to the singular geometry mapping. To prevent these highly stretched elements, we can replace the tensor product meshes used so far by hierarchical meshes. In Fig. 12, we illustrate the hierarchical mesh scheme exemplarily for the unit disk with crack in combination with both uniform and graded refinement. Again, this serves as a prototype for other circular sectors. Note that the refinement is fixed a priori and not chosen in an adaptive way as it is typically the case in the context of

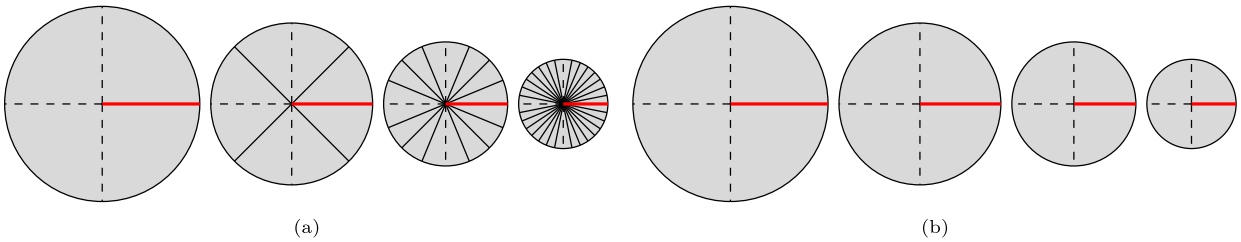

Fig. 13. Sketch of the physical mesh elements near the conical point during refinement. (a) tensor product refinement. (b) hierarchical refinement. The scaling between the refinement steps is manipulated for better visibility.

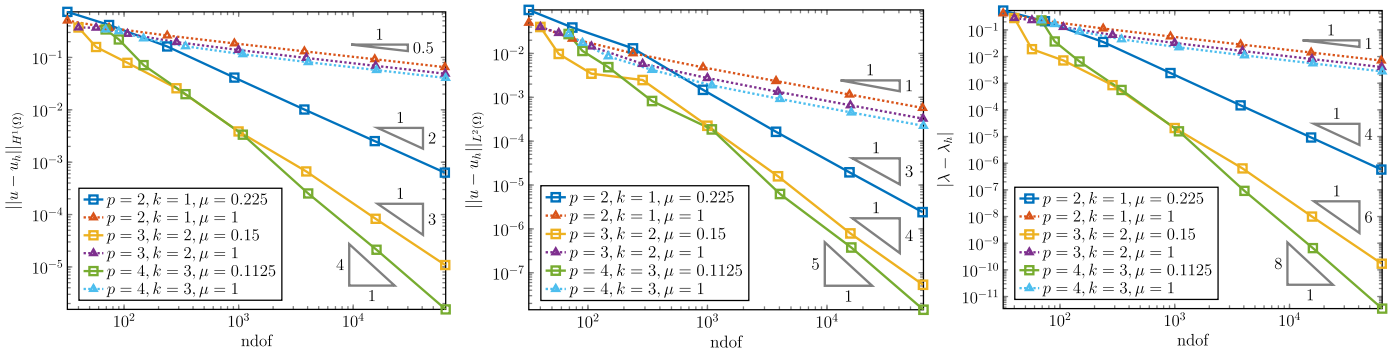

Fig. 14. Approximation errors for the eigenfunction $u=u_{\nu_1,1}$ and its corresponding eigenvalue $\lambda=\lambda_{\nu_1,1}$ using gradually and uniformly refined hierarchical NURBS of degree $\boldsymbol{p}=(p,p)$, $p\in\{2,3,4\}$, and regularity $\boldsymbol{k}=(p-1,p-1)$. We set $\mu=0.9\frac{\nu_1}{p}=\frac{0.9}{2p}$ for graded meshes and $\mu=1$ corresponds to uniform refinement.

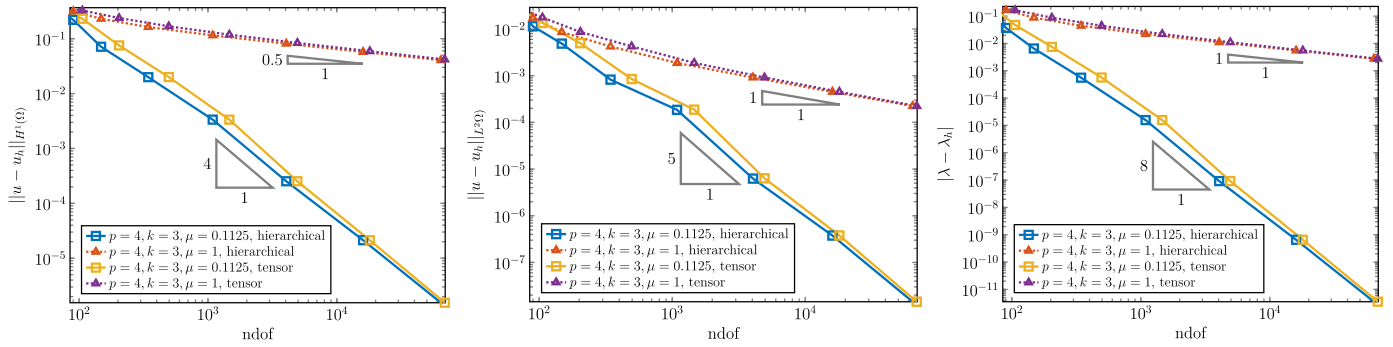

Fig. 15. Approximation errors for the eigenfunction $u=u_{\nu_1,1}$ and its corresponding eigenvalue $\lambda=\lambda_{\nu_1,1}$ using NURBS of degree $\boldsymbol{p}=(4,4)$ and regularity $\boldsymbol{k}=(3,3)$ on tensor product and hierarchical meshes. We set $\mu=0.9\frac{\nu_1}{4}=0.1125$ for graded meshes and $\mu=1$ corresponds to uniform refinement.

hierarchical splines. Similar ideas have been mentioned in the context of singularly parameterized triangles [45], subdivision based isogeometric analysis [61], or finite element methods on spherical domains [62]. In GeoPDEs, the hierarchical refinement scheme can be implemented by using the extension of the package presented in [63]. It leads to a purely isotropic mesh in the physical domain; the corresponding aspect ratio (4.10) simplifies to

$$\frac{h_1^{1/\mu}}{h_1^{1/\mu}}=1\,.$$

Besides, the hierarchical meshes offer another advantage. As outlined in Section 4.3, the physical approximation space has to be modified since the standard basis functions associated to the control points in the center of the circular sector do not belong to the solution space of the weak problem. By employing a hierarchical approach, the number of mesh elements in the vicinity of the conical point and thus the number of such problematic basis functions is held constant over the refinement steps, which is not the case for standard tensor product refinement. We visualize this effect in Fig. 13.

In the following numerical examples, we test the described hierarchical approach for approximating the Laplace eigenvalues and eigenfunctions of circular sectors.

Example 5.7 *(Eigenfunction of type (A))*. We perform the same experiment as in Example 5.1, this time employing a hierarchical refinement approach. In more detail, we compute the eigenvalue $\lambda_{\nu_1,1}$ of the unit disk with crack and its corresponding eigenfunction $u_{\nu_1,1}$, which is characterized by its low regularity, on both uniform and graded hierarchical meshes. The approximation errors for NURBS of polynomial degree $\boldsymbol{p}=(p,p)$, where $p\in\{2,3,4\}$, and regularity $\boldsymbol{k}=(p-1,p-1)$ are presented in Fig. 14 and closely resemble those obtained with tensor product meshes in Fig. 8. Optimal convergence rates for the $H^1(\Omega)$- and $L^2(\Omega)$-error of the eigenfunction and the absolute eigenvalue error are recovered by using an appropriate grading parameter. An explicit comparison of the approximation errors generated by hierarchical and tensor product meshes is depicted in Fig. 15, where NURBS of degree $\boldsymbol{p}=(4,4)$ and regularity $\boldsymbol{k}=(3,3)$ are refined gradually and uniformly with grading parameters $\mu=0.9\cdot\frac{\nu_1}{4}=0.1125$ and $\mu=1$, respectively. The results indicate that the approximation constant of hierarchical meshes is slightly better than the one of tensor product meshes. This ef-

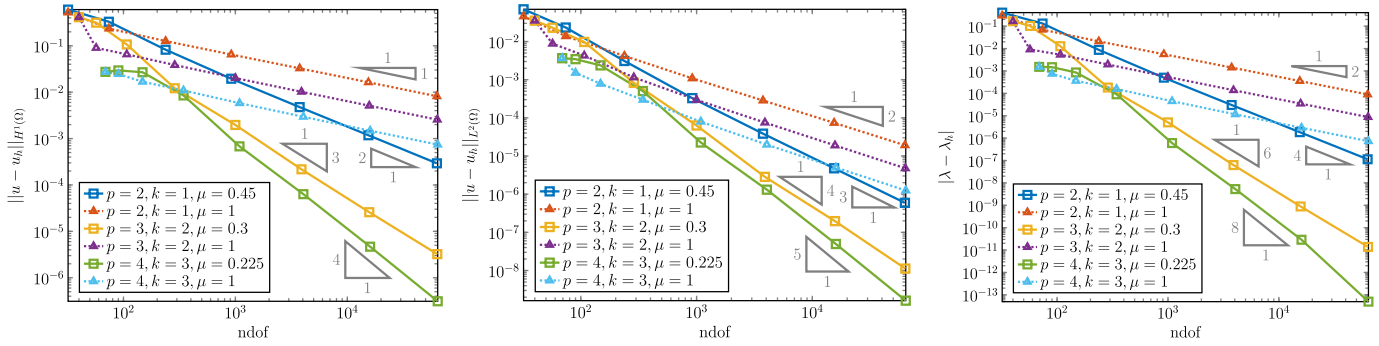

Fig. 16. Approximation errors for the eigenfunction $u = u_{\nu_2,1}$ and its corresponding eigenvalue $\lambda = \lambda_{\nu_2,1}$ using gradually and uniformly refined hierarchical NURBS of degree $\boldsymbol{p} = (p,p)$, $p \in \{2,3,4\}$, and regularity $\boldsymbol{k} = (p-1, p-1)$. We set $\mu = 0.9\frac{\nu_2}{p} = \frac{0.9}{p}$ for graded meshes and $\mu = 1$ corresponds to uniform refinement.

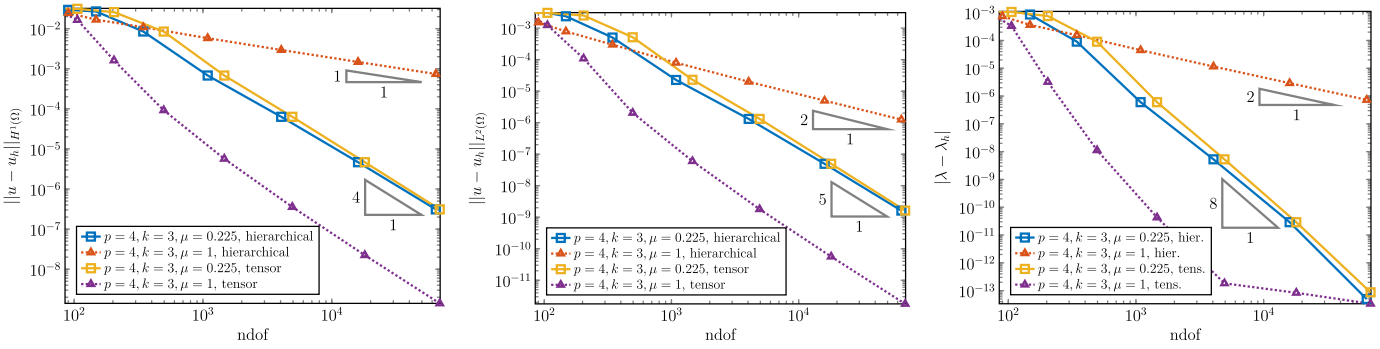

Fig. 17. Approximation errors for the eigenfunction $u = u_{\nu_2,1}$ and its corresponding eigenvalue $\lambda = \lambda_{\nu_2,1}$ using NURBS of degree $\boldsymbol{p} = (4,4)$ and regularity $\boldsymbol{k} = (3,3)$ on tensor product and hierarchical meshes. We set $\mu = 0.9\frac{\nu_2}{4} = 0.225$ for graded meshes and $\mu = 1$ corresponds to uniform refinement.

fect can be explained by the omission of redundant degrees of freedom during the hierarchical refinement procedure. As illustrated in Fig. 13, the circular elements close to the singularity are subdivided fewer times while the same approximation accuracy is achieved.

Example 5.8 *(Eigenfunction of type (B))*. Finally, we repeat the experiment from Example 5.2, but now using the hierarchical refinement scheme. We approximate the smooth eigenfunction $u_{\nu_2,1}$ and its corresponding eigenvalue $\lambda_{\nu_2,1}$ of the unit disk with crack on both uniform and graded hierarchical meshes. The approximation errors for NURBS of polynomial degree $\boldsymbol{p} = (p,p)$, where $p \in \{2,3,4\}$, and regularity $\boldsymbol{k} = (p-1, p-1)$ are illustrated in Fig. 16 and clearly differ from the ones obtained with tensor product refinement in Fig. 9. Independent from the NURBS degree, the convergence rates for the $H^1(\Omega)$- and $L^2(\Omega)$-error of the eigenfunction and the absolute eigenvalue error generated by uniform hierarchical refinement are 1, 2 and 2, respectively, and thus not optimal. In contrast, graded hierarchical meshes do produce optimal convergence rates of p, $p+1$ and $2p$, respectively. The different precisions obtained with hierarchical and tensor product meshes are demonstrated explicitly in Fig. 17, where NURBS of degree $\boldsymbol{p} = (4,4)$ and regularity $\boldsymbol{k} = (3,3)$ are refined both gradually and uniformly with grading parameters $\mu = 0.9 \cdot \frac{\nu_1}{4} = 0.1125$ and $\mu = 1$, respectively. These results indicate that mesh grading restores optimal convergence of the hierarchically refined solutions. However, in this case, the grading is not required by the regularity of the approximated eigenfunction but by the hierarchical structure of the mesh, which is consistent with the theoretical findings in [61]. This is because the size of the hierarchical mesh elements close to the singularity, as illustrated in Fig. 13b, does not decrease fast enough during uniform refinement. Yet, with sufficiently strong mesh grading towards the singularity, this issue is addressed.

Next, we perform a numerical test to assess the optimal grading parameter for hierarchical meshes. The results for eigenfunctions of type (A) are very similar to the ones for tensor product meshes shown in Section 5.3 and are thus not carried out again here. However, as shown in Example 5.8, the approximation properties of hierarchical meshes differ for eigenfunctions of type (B), which is why we investigate the optimal grading parameter for this setting in the following example.

Example 5.9. We approximate the eigenvalue $\lambda_{\nu_2,1}$ of the unit disk with crack and its corresponding smooth eigenfunction $u_{\nu_2,1}$, this time using gradually refined NURBS of degree $\boldsymbol{p} = (2,2)$ and regularity $\boldsymbol{k} = (1,1)$ with different grading parameters μ. In Tables 6 and 7, we list the $H^1(\Omega)$-errors of the eigenfunction and the absolute eigenvalue errors, respectively, together with the corresponding experimental convergence rates. We observe suboptimal convergence orders for grading parameters $\mu > \frac{\nu_2}{p}$ and optimal rates for $\mu < \frac{\nu_2}{p}$. Among the sufficiently graded meshes, the moderate grading with $\mu = 0.9\frac{\nu_2}{p}$ is preferable over the strong grading with $\mu = 0.7\frac{\nu_2}{p}$ due to an improved approximation constant.

Similar investigations as in Example 5.9 can be carried out for further eigenfunctions of type (B) and lead to comparable results. Thus, we conclude that the recommended grading parameter for the approximation of a specific eigenfunction $u_{\nu_k,m}$ on hierarchical meshes is

$$\mu = 0.9\frac{\nu_k}{p}.$$

Note that there is a heavy difference to the previous recommendation (4.13) for tensor product meshes, since the approximation of all eigenfunctions, independently of their regularity, requires an appropriate grading of the mesh.

In summary, the combination of the presented hierarchical mesh structure and graded refinement is very promising for approximating the Laplace eigenvalues of circular sectors and their corresponding eigenfunctions of both type (A) and type (B). However, the implementation

Table 6
Approximation errors $\|u-u_h\|_{H^1(\Omega)}$ (and corresponding experimental orders of convergence) for the eigenfunction $u=u_{\nu_2,1}$ using gradually refined hierarchical NURBS of degree $\boldsymbol{p}=(2,2)$ and regularity $\boldsymbol{k}=(1,1)$ with different grading parameters μ.

ndof	$\mu=0.7\frac{\nu_2}{p}=0.35$	$\mu=0.9\frac{\nu_2}{p}=0.45$	$\mu=1.1\frac{\nu_2}{p}=0.55$	$\mu=1.3\frac{\nu_2}{p}=0.65$
32	5.6582e − 01	6.0335e − 01	6.1669e − 01	6.1087e − 01
74	4.3238e − 01 (0.75)	3.3039e − 01 (1.68)	2.6714e − 01 (2.33)	2.3424e − 01 (2.67)
238	1.2868e − 01 (2.21)	8.2363e − 02 (2.53)	6.7629e − 02 (2.50)	7.1675e − 02 (2.16)
918	3.0357e − 02 (2.18)	1.9502e − 02 (2.17)	1.7540e − 02 (2.04)	2.2973e − 02 (1.72)
3750	7.4289e − 03 (2.01)	4.7691e − 03 (2.01)	4.6465e − 03 (1.90)	7.5817e − 03 (1.58)
15430	1.8469e − 03 (1.97)	1.1794e − 03 (1.98)	1.2449e − 03 (1.86)	2.5485e − 03 (1.54)
63110	4.6106e − 04 (1.97)	2.9289e − 04 (1.98)	3.3634e − 04 (1.86)	8.6597e − 04 (1.53)
256262	1.1522e − 04 (1.98)	7.2890e − 05 (1.99)	9.1552e − 05 (1.86)	2.9603e − 04 (1.53)

Table 7
Approximation errors $|\lambda-\lambda_h|$ (and corresponding experimental orders of convergence) for the eigenvalue $\lambda=\lambda_{\nu_2,1}$ using gradually refined hierarchical NURBS of degree $\boldsymbol{p}=(2,2)$ and regularity $\boldsymbol{k}=(1,1)$ with different grading parameters μ.

ndof	$\mu=0.7\frac{\nu_2}{p}=0.35$	$\mu=0.9\frac{\nu_2}{p}=0.45$	$\mu=1.1\frac{\nu_2}{p}=0.55$	$\mu=1.3\frac{\nu_2}{p}=0.65$
32	4.0667e − 01	4.0420e − 01	3.9597e − 01	3.8085e − 01
74	2.0471e − 01 (1.91)	1.3166e − 01 (3.13)	8.8493e − 02 (4.17)	6.9630e − 02 (4.73)
238	2.0781e − 02 (4.16)	8.7422e − 03 (4.94)	5.9965e − 03 (4.90)	6.7821e − 03 (4.24)
918	1.2085e − 03 (4.29)	5.0176e − 04 (4.31)	4.0802e − 04 (4.06)	7.0223e − 04 (3.42)
3750	7.3097e − 05 (4.01)	3.0168e − 05 (4.01)	2.8704e − 05 (3.79)	7.6576e − 05 (3.16)
15430	4.5285e − 06 (3.94)	1.8474e − 06 (3.95)	2.0615e − 06 (3.73)	8.6548e − 06 (3.09)
63110	2.8239e − 07 (3.94)	1.1397e − 07 (3.96)	1.5053e − 07 (3.72)	9.9936e − 07 (3.07)
256262	1.7639e − 08 (3.96)	7.0592e − 09 (3.97)	1.1154e − 08 (3.71)	1.1679e − 07 (3.06)

and mathematical analysis are more difficult. Our numerical results can be a starting point for further investigations, especially in context with the theoretical explanations in [61].

6. Conclusion and outlook

In this paper, we studied the Laplace eigenvalue problem on circular sectors both analytically and numerically. We verified crucial regularity properties of the exact eigenfunctions and developed an effective numerical method to address the occurring singularities. In particular, we introduced a single-patch graded mesh refinement algorithm for isogeometric analysis on circular sectors, enabling local refinement towards the conical point, where some of the eigenfunctions show singular behavior. Since the polar-like isogeometric parameterization of circular sectors is also singular at the conical point, a modified approximation space is used. We demonstrated optimal convergence rates for the eigenvalues and eigenfunctions numerically. Furthermore, we illustrated that smooth splines have a better approximation constant than their C^0-continuous counterparts on both uniform and graded meshes, at least for the lower part of the Laplace spectrum. Hence, we were able to extend some of the excellent spectral approximation properties of smooth splines, which have been discovered in the literature mainly for domains of rectangular nature, to circular sectors. In addition, we demonstrated the power of smooth splines on graded meshes for an accurate approximation of the 100 smallest eigenvalues. Lastly, we considered a hierarchical refinement approach to avoid anisotropic elements in the physical Bézier mesh. We showed the efficiency of graded hierarchical meshes to simulate eigenfunctions with and without singularities and compared them with the previously used tensor product meshes. Here, we observed two advantages of the hierarchical scheme: redundant degrees of freedom are omitted and the number of mesh elements in the vicinity of the conical point is held constant.

This contribution serves as motivation for various directions of further research. In general, we are lacking theoretical error estimates for isogeometric analysis on singularly parameterized circular sectors, both for tensor product and hierarchical meshes. We aim to address this gap in future work and, specifically, prove optimal approximation of non-smooth functions using our graded refinement algorithm. In addition, the presented method is extendable to other eigenvalue and boundary value problems on arbitrary two-dimensional single-patch domains with corner singularities. Here, our results serve as a proof of concept since the local neighborhood of a singular point can always be described by a circular sector. More work remains to be done for an extension of the method to multi-patch IGA and three-dimensional bodies with corner and edge singularities. Besides, it is well-established in finite element analysis that the hp-method is effective for handling singularities. Therefore, another idea for future research is to explore the p- and k-versions of graded refinement or to consider graded multi-degree polar splines [50]. Finally, our findings provide a basis for future work on spectral approximation properties of smooth splines on circular sectors and, more generally, of singularly parameterized domains. Particularly, the appearance of spectral branches and the approximation constant in the upper part of the discrete spectrum remain to be investigated.

Data availability

Data will be made available on request.

Acknowledgements

The authors thank Thomas Takacs, Alessandro Reali and Volker Kempf for motivating and insightful scientific discussions which helped to place the results of this paper within the existing literature context. Moreover, the authors express their gratitude to Rafael Vázquez for providing an open-source software package for isogeometric analysis and for his prompt assistance with any related questions. Finally, we thank the anonymous referees for their comments which led to an improvement of the paper.

Appendix A. Explicit representation of the single-patch parameterization

To gain a better understanding, we indicate an explicit representation of the single-patch parameterization of the unit disk with crack that is used throughout this paper. It can be shown that the weight function (3.2) only depends on ζ_2,

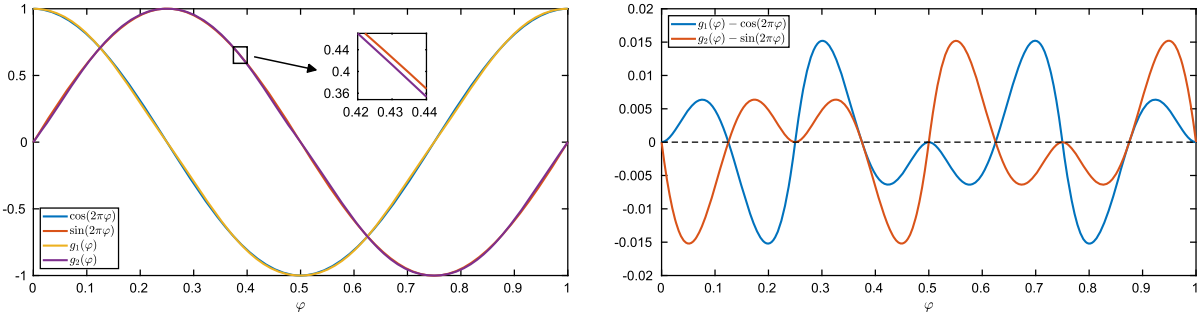

Fig. B.18. (a): Isogeometric mappings g_1 and g_2 versus scaled polar angular mappings. (b): Difference between the corresponding functions.

$$W(\zeta) = \sum_{i_1=1}^{2} \widehat{B}_{i_1,1}(\zeta_1) \sum_{i_2=2}^{9} \widehat{B}_{i_2,2}(\zeta_2)\, w_{(2,i_2)} \equiv w(\zeta_2),$$

and is bounded away from zero,

$$\frac{2+\sqrt{2}}{4} \le W(\zeta_1,\zeta_2) \equiv w(\zeta_2) \le 1,$$

see [19,20] for more details. By inserting the control points c_i, we obtain a compact representation of the resulting NURBS parameterization $\boldsymbol{F}: \widehat{\Omega} \to \Omega$,

$$\begin{aligned} \boldsymbol{F}(\zeta) &= \sum_{i_1=1}^{2} \sum_{i_2=1}^{9} \boldsymbol{c}_{(i_1,i_2)} \frac{w_{(i_1,i_2)}\, \widehat{B}_{i_1,1}(\zeta_1)\, \widehat{B}_{i_2,2}(\zeta_2)}{w(\zeta_2)} \\ &= \zeta_1 \sum_{i_2=1}^{9} \boldsymbol{c}_{(2,i_2)} \frac{w_{(2,i_2)}\, \widehat{B}_{i_2,2}(\zeta_2)}{w(\zeta_2)} \\ &=: \zeta_1 \left(g_1(\zeta_2), g_2(\zeta_2)\right)^T, \end{aligned} \tag{A.1}$$

with functions $g_1, g_2 : [0,1] \to \mathbb{R}$ depending only on ζ_2.

Appendix B. Comparison with polar coordinates

As the geometry mapping $\boldsymbol{F}$ resembles the classic transformation from polar to Cartesian coordinates,

$$\mathring{\boldsymbol{F}}: (0,1)\times(0,2\pi) \to \Omega,\ (r,\varphi) \mapsto (r\cos\varphi, r\sin\varphi),$$

we point out some properties to compare the two parameterizations. First, let $(r,\varphi) \in (0,1)\times(0,2\pi)$ and $(\zeta_1,\zeta_2) \in (0,1)\times(0,1)$ such that $\mathring{\boldsymbol{F}}(r,\varphi) = \boldsymbol{F}(\zeta_1,\zeta_2)$. Using the representation (A.1) of $\boldsymbol{F}$ and the fact that $\left(g_1(\zeta_2)\right)^2 + \left(g_2(\zeta_2)\right)^2 = 1$ for all $\zeta_2 \in [0,1]$, see [20], it follows that

$$r = |\mathring{\boldsymbol{F}}(r,\varphi)| = \left|\boldsymbol{F}(\zeta_1,\zeta_2)\right| = \zeta_1 \left(\left(g_1(\zeta_2)\right)^{(2)} + \left(g_2(\zeta_2)\right)^{(2)}\right) = \zeta_1.$$

Hence, the radial component r in polar coordinates corresponds one-to-one with the isogeometric ζ_1-component. However, the same does not apply for the angular components φ and ζ_2. Fig. B.18a presents the isogeometric mappings g_1 and g_2 from representation (A.1) in comparison with the scaled polar angular mappings $[0,1] \to \mathbb{R},\ \varphi \mapsto \cos(2\pi\varphi)$ and $[0,1] \to \mathbb{R},\ \varphi \mapsto \sin(2\pi\varphi)$. Fig. B.18b depicts the difference of the corresponding functions. We observe that

$$\left|g_1(\varphi) - \cos(2\pi\varphi)\right| \le C \quad \text{and} \quad \left|g_2(\varphi) - \sin(2\pi\varphi)\right| \le C \text{ for all } \varphi \in [0,1],$$

that is, the parameterizations coincide up to a maximal difference of $C \approx 0.015$. The mappings are even identical in a few points,

$$g_1(\varphi) = \cos(2\pi\varphi) \quad \text{and} \quad g_2(\varphi) = \sin(2\pi\varphi) \text{ for } \varphi = \frac{i}{8}, i = 0,\dots,8. \tag{B.1}$$

Furthermore, we can show another useful correlation. Let $K = \boldsymbol{F}(Q) \in \mathcal{M}$ be an element of the Bézier mesh. Then, K can be represented in polar coordinates, that is, we can find $\mathring{Q} \subset (0,1)\times(0,2\pi)$ such that

$$K = \boldsymbol{F}(Q) = \mathring{\boldsymbol{F}}\left(\mathring{Q}\right).$$

In more detail, if $Q = Q_j = \left(\zeta_{1,j_1}, \zeta_{1,j_1+1}\right) \times \left(\zeta_{2,j_2}, \zeta_{2,j_2+1}\right)$ for some $j \in \boldsymbol{J}$, there are polar angles $\varphi_{j_2}, \varphi_{j_2+1} \in [0,2\pi]$ such that $\mathring{Q} = \left(\zeta_{1,j_1}, \zeta_{1,j_1+1}\right) \times \left(\varphi_{j_2}, \varphi_{j_2+1}\right)$. This can be proven using the bijectivity of the parameterizations away from the singular edge $\{(0,\zeta_2) : \zeta_2 \in [0,1]\}$.

References

[1] M. Kac, Can one hear the shape of a drum?, Am. Math. Mon. 73 (1966) 1–23, https://doi.org/10.2307/2313748.

[2] M. Reuter, F.-E. Wolter, N. Peinecke, Laplace-Beltrami spectra as 'Shape-DNA' of surfaces and solids, Comput. Aided Des. 38 (2006) 342–366, https://doi.org/10.1016/j.cad.2005.10.011.

[3] I. Babuška, J. Osborn, Eigenvalue problems, in: Finite Element Methods (Part 1), in: Handbook of Numerical Analysis, vol. 2, Elsevier, 1991, pp. 641–787.

[4] A. Clebsch, Theorie der Elasticität Fester Körper, Teubner, Leipzig, 1862.

[5] Lord Rayleigh (J. W. Strutt), The Theory of Sound, second ed., Dover Publications, New York, 1945.

[6] W.A. Strauss, Partial Differential Equations: An Introduction, second ed., John Wiley & Sons, Ltd., Chichester, 2008.

[7] J.A. Cottrell, A. Reali, Y. Bazilevs, T.J.R. Hughes, Isogeometric analysis of structural vibrations, Comput. Methods Appl. Mech. Eng. 195 (2006) 5257–5296, https://doi.org/10.1016/j.cma.2005.09.027.

[8] T.J.R. Hughes, A. Reali, G. Sangalli, Duality and unified analysis of discrete approximations in structural dynamics and wave propagation: comparison of *p*-method finite elements with *k*-method NURBS, Comput. Methods Appl. Mech. Eng. 197 (2008) 4104–4124, https://doi.org/10.1016/j.cma.2008.04.006.

[9] J.A. Cottrell, T.J.R. Hughes, Y. Bazilevs, Isogeometric Analysis. Toward Integration of CAD and FEA, John Wiley & Sons, Ltd., Chichester, 2009.

[10] J.A. Cottrell, T.J.R. Hughes, A. Reali, Studies of refinement and continuity in isogeometric structural analysis, Comput. Methods Appl. Mech. Eng. 196 (2007) 4160–4183, https://doi.org/10.1016/j.cma.2007.04.007.

[11] T.J.R. Hughes, J.A. Evans, A. Reali, Finite element and NURBS approximations of eigenvalue, boundary-value, and initial-value problems, Comput. Methods Appl. Mech. Eng. 272 (2014) 290–320, https://doi.org/10.1016/j.cma.2013.11.012.

[12] E. Sande, C. Manni, H. Speleers, Sharp error estimates for spline approximation: explicit constants, *n*-widths, and eigenfunction convergence, Math. Models Methods Appl. Sci. 29 (2019) 1175–1205, https://doi.org/10.1142/S0218202519500192.

[13] E. Sande, C. Manni, H. Speleers, Explicit error estimates for spline approximation of arbitrary smoothness in isogeometric analysis, Numer. Math. 144 (2020) 889–929, https://doi.org/10.1007/s00211-019-01097-9.

[14] R.R. Hiemstra, T.J.R. Hughes, A. Reali, D. Schillinger, Removal of spurious outlier frequencies and modes from isogeometric discretizations of second- and fourth-order problems in one, two, and three dimensions, Comput. Methods Appl. Mech. Eng. 387 (2021) 114115, https://doi.org/10.1016/j.cma.2021.114115.

[15] C. Manni, E. Sande, H. Speleers, Application of optimal spline subspaces for the removal of spurious outliers in isogeometric discretizations, Comput. Methods Appl. Mech. Eng. 389 (2022) 114260, https://doi.org/10.1016/j.cma.2021.114260.

[16] T.J.R. Hughes, J.A. Cottrell, Y. Bazilevs, Isogeometric analysis: CAD, finite elements, NURBS, exact geometry and mesh refinement, Comput. Methods Appl. Mech. Eng. 194 (2005) 4135–4195, https://doi.org/10.1016/j.cma.2004.10.008.

[17] J. Lu, Circular element: isogeometric elements of smooth boundary, Comput. Methods Appl. Mech. Eng. 198 (2009) 2391–2402, https://doi.org/10.1016/j.cma.2009.02.029.

[18] Z.C. Li, T.T. Lu, Singularities and treatments of elliptic boundary value problems, Math. Comput. Model. 31 (2000) 97–145, https://doi.org/10.1016/S0895-7177(00)00062-5.

[19] J.W. Jeong, H.-S. Oh, S. Kang, H. Kim, Mapping techniques for isogeometric analysis of elliptic boundary value problems containing singularities, Comput. Methods Appl. Mech. Eng. 254 (2013) 334–352, https://doi.org/10.1016/j.cma.2012.09.009.
[20] H.-S. Oh, H. Kim, J.W. Jeong, Enriched isogeometric analysis of elliptic boundary value problems in domains with cracks and/or corners, Int. J. Numer. Methods Eng. 97 (2014) 149–180, https://doi.org/10.1002/nme.4580.
[21] T. Jonsson, M.G. Larson, K. Larsson, Graded parametric CutFEM and CutIGA for elliptic boundary value problems in domains with corners, Comput. Methods Appl. Mech. Eng. 354 (2019) 331–350, https://doi.org/10.1016/j.cma.2019.05.024.
[22] A. Buffa, G. Gantner, C. Giannelli, D. Praetorius, R. Vázquez, Mathematical foundations of adaptive isogeometric analysis, Arch. Comput. Methods Eng. 29 (2022) 4479–4555, https://doi.org/10.1007/s11831-022-09752-5.
[23] B. Marussig, T.J.R. Hughes, A review of trimming in isogeometric analysis: challenges, data exchange and simulation aspects, Arch. Comput. Methods Eng. 25 (2018) 1059–1127, https://doi.org/10.1007/s11831-017-9220-9.
[24] T. Apel, A.-M. Sändig, J.R. Whiteman, Graded mesh refinement and error estimates for finite element solutions of elliptic boundary value problems in non-smooth domains, Math. Methods Appl. Sci. 19 (1996) 63–85, https://doi.org/10.1002/(SICI)1099-1476(19960110)19:1<63::AID-MMA764>3.0.CO;2-S.
[25] T. Apel, S. Nicaise, The finite element method with anisotropic mesh grading for elliptic problems in domains with corners and edges, Math. Methods Appl. Sci. 21 (1998) 519–549, https://doi.org/10.1002/(SICI)1099-1476(199804)21:6<519::AID-MMA962>3.0.CO;2-R.
[26] I. Babuška, Finite element method for domains with corners, Computing 6 (1970) 264–273, https://doi.org/10.1007/bf02238811.
[27] L.A. Oganesjan, L.A. Rukhovets, Variational-difference schemes for linear second-order elliptic equations in a two-dimensional region with piecewise smooth boundary, Ž. Vyčisl. Mat. Mat. Fiz. 8 (1968) 97–114 (in Russian). English translation in USSR Comput. Math. Math. Phys. 8 (1968) 129–152.
[28] U. Langer, A. Mantzaflaris, S.E. Moore, I. Toulopoulos, Mesh grading in isogeometric analysis, Comput. Math. Appl. 70 (2015) 1685–1700, https://doi.org/10.1016/j.camwa.2015.03.011.
[29] T. Takacs, B. Jüttler, Existence of stiffness matrix integrals for singularly parameterized domains in isogeometric analysis, Comput. Methods Appl. Mech. Eng. 200 (2011) 3568–3582, https://doi.org/10.1016/j.cma.2011.08.023.
[30] T. Takacs, B. Jüttler, H^2 regularity properties of singular parameterizations in isogeometric analysis, Graph. Models 74 (2012) 361–372, https://doi.org/10.1016/j.gmod.2012.05.006.
[31] T. Takacs, Construction of smooth isogeometric function spaces on singularly parameterized domains, in: Curves and Surfaces, in: Lecture Notes in Comput. Sci., vol. 9213, Springer, Cham, 2015, pp. 433–451.
[32] T. Takacs, Approximation properties of isogeometric function spaces on singularly parameterized domains, arXiv:1507.08095, 2015.
[33] J.R. Kuttler, V.G. Sigillito, Eigenvalues of the Laplacian in two dimensions, SIAM Rev. 26 (1984) 163–193, https://doi.org/10.1137/1026033.
[34] D.S. Grebenkov, B.-T. Nguyen, Geometrical structure of Laplacian eigenfunctions, SIAM Rev. 55 (2013) 601–667, https://doi.org/10.1137/120880173.
[35] M. Abramowitz, I.A. Stegun, R.H. Romer, Handbook of Mathematical Functions with Formulas, Graphs, and Mathematical Tables, vol. 56, 1988.
[36] G.N. Watson, A Treatise on the Theory of Bessel Functions, Cambridge Mathematical Library, second ed., Cambridge University Press, Cambridge, 1995.
[37] A. Elbert, Some recent results on the zeros of Bessel functions and orthogonal polynomials, J. Comput. Appl. Math. 133 (2001) 65–83, https://doi.org/10.1016/S0377-0427(00)00635-X.
[38] F.W.J. Olver, A further method for the evaluation of zeros of Bessel functions and some new asymptotic expansions for zeros of functions of large order, Proc. Camb. Philos. Soc. 47 (1951) 699–712, https://doi.org/10.1017/S0305004100027158.
[39] F.W.J. Olver, Some new asymptotic expansions for Bessel functions of large orders, Proc. Camb. Philos. Soc. 48 (1952) 414–427, https://doi.org/10.1017/S030500410002781X.
[40] I.N. Bronstein, K.A. Semendjajew, G. Musiol, H. Mühlig, Taschenbuch der Mathematik, Verlag Harri Deutsch, Thun, 2001.
[41] L. Beirão da Veiga, A. Buffa, G. Sangalli, R. Vázquez, Mathematical analysis of variational isogeometric methods, Acta Numer. 23 (2014) 157–287, https://doi.org/10.1017/S096249291400004X.
[42] L.L. Schumaker, Spline Functions: Basic Theory, Cambridge Mathematical Library, third ed., Cambridge University Press, Cambridge, 2007.
[43] L. Piegl, W. Tiller, The NURBS Book, Springer, Berlin, Heidelberg, 1995.
[44] G.E. Farin, NURB Curves and Surfaces: from Projective Geometry to Practical Use, A. K. Peters, Ltd., Wellesley, MA, 1995.
[45] T. Takacs, Singularities in isogeometric analysis, in: Civil-Comp Proceedings 100, 2012.
[46] T. Nguyen, K. Karčiauskas, J. Peters, A comparative study of several classical, discrete differential and isogeometric methods for solving Poisson's equation on the disk, Axioms 3 (2014) 280–299, https://doi.org/10.3390/axioms3020280.
[47] T.J.R. Hughes, G. Sangalli, Mathematics of Isogeometric Analysis: A Conspectus, John Wiley & Sons, Ltd., 2017, pp. 1–40.
[48] Y. Bazilevs, L. Beirão da Veiga, J.A. Cottrell, T.J.R. Hughes, G. Sangalli, Isogeometric analysis: approximation, stability and error estimates for h-refined meshes, Math. Models Methods Appl. Sci. 16 (2006) 1031–1090, https://doi.org/10.1142/S0218202506001455.
[49] L. Beirão da Veiga, D. Cho, G. Sangalli, Anisotropic NURBS approximation in isogeometric analysis, Comput. Methods Appl. Mech. Eng. 209 (212) (2012) 1–11, https://doi.org/10.1016/j.cma.2011.10.016.
[50] D. Toshniwal, H. Speleers, R.R. Hiemstra, T.J. Hughes, Multi-degree smooth polar splines: a framework for geometric modeling and isogeometric analysis, Comput. Methods Appl. Mech. Eng. 316 (2017) 1005–1061, https://doi.org/10.1016/j.cma.2016.11.009.
[51] T. Apel, P. Zilk, Isogeometric analysis of the Laplace eigenvalue problem on circular sectors: regularity properties, graded meshes & variational crimes, arXiv:2402.16589, 2024.
[52] T. Apel, J.M. Melenk, Interpolation and quasi-interpolation in h- and hp-version finite element spaces, in: eds E. Stein, R. Borst, T.J.R. Hughes (Eds.), Encyclopedia of Computational Mechanics, second edition, John Wiley & Sons, Ltd., Chichester, 2017, pp. 1–33.
[53] I. Babuška, A.K. Aziz, Survey lectures on the mathematical foundations of the finite element method, in: The Mathematical Foundations of the Finite Element Method with Applications to Partial Differential Equations, Proc. Sympos., Univ. Maryland, Baltimore, Md., 1972, Academic Press, New York, 1972, pp. 1–359.
[54] D. Boffi, Finite element approximation of eigenvalue problems, Acta Numer. 19 (2010) 1–120, https://doi.org/10.1017/S0962492910000012.
[55] R. Vázquez, A new design for the implementation of isogeometric analysis in Octave and Matlab: GeoPDEs 3.0, Comput. Math. Appl. 72 (2016) 523–554, https://doi.org/10.1016/j.camwa.2016.05.010.
[56] C. de Falco, A. Reali, R. Vázquez, GeoPDEs: a research tool for isogeometric analysis of PDEs, Adv. Eng. Softw. 42 (2011) 1020–1034, https://doi.org/10.1016/j.advengsoft.2011.06.010.
[57] A. Bartezzaghi, L. Dedè, A. Quarteroni, Isogeometric analysis of high order partial differential equations on surfaces, Comput. Methods Appl. Mech. Eng. 295 (2015) 446–469, https://doi.org/10.1016/j.cma.2015.07.018.
[58] S. Giani, L. Grubišić, H. Hakula, J.S. Ovall, A posteriori error estimates for elliptic eigenvalue problems using auxiliary subspace techniques, J. Sci. Comput. 88 (2021) 55, https://doi.org/10.1007/s10915-021-01572-2.
[59] G. Strang, G. Fix, An Analysis of the Finite Element Method, second ed., Wellesley-Cambridge Press, Wellesley, MA, 2008.
[60] T.J. Hughes, The Finite Element Method: Linear Static and Dynamic Finite Element Analysis, Dover Publications, Mineola, NY, 2012.
[61] T. Takacs, Approximation properties over self-similar meshes of curved finite elements and applications to subdivision based isogeometric analysis, arXiv:2307.10403, 2023.
[62] T. Apel, C. Pester, Clement-type interpolation on spherical domains—interpolation error estimates and application to a posteriori error estimation, IMA J. Numer. Anal. 25 (2005) 310–336, https://doi.org/10.1093/imanum/drh024.
[63] E.M. Garau, R. Vázquez, Algorithms for the implementation of adaptive isogeometric methods using hierarchical B-splines, Appl. Numer. Math. 123 (2018) 58–87, https://doi.org/10.1016/j.apnum.2017.08.006.